Evaluation and Sub-selection of CMIP6 GCMs over Southeast Asia for Dynamical Downscaling

5

Authors:
Aurel Florian Moise, Sandeep Sahany, Muhammad Eeqmal Hassim, Chen Chen, Xin Rong Chua, Venkatraman Prasanna, Gerald Lim, Pavan Harika Raavi, Fei Luo

Meteorological Service Singapore
Centre for Climate Research Singapore

5.1 Introduction

The Southeast Asia (SEA) region is home to ca. 8.5% of the global population and is highly vulnerable to climate change both due to the projected increase in natural hazards and the limited adaptive capacity of many of the SEA countries. The weather and climate over SEA are influenced by many local, regional, and large-scale processes. Some of the important large scale processes include the Asian-Australian monsoon system, the Madden Julian Oscillation (MJO), El-Nino Southern Oscillation (ENSO), Indian Ocean Dipole (IOD), etc. Even within this region there is a large variation in the climatic conditions both in terms of mean and variability.

In line with the previous generations of the Coupled Model Intercomparison Projects (CMIPs), the CMIP6 (Eyring et al, 2016) provides us with a coordinated set of climate model simulations from climate modelling centres around the world. Although global models have been known to perform well in providing large scale climate information, such as global mean temperature and rainfall, the regional and local climatic features are more prone to biases.

According to the Sixth Assessment Report (AR6) by the Intergovernmental Panel on Climate Change (IPCC) the CMIP6 multi-model mean is cooler over the period 1980-2000 than both observations and CMIP5 (Bock et al., 2020; Flynn and Mauritsen, 2020), and that these biases of several tenths of a degree in some CMIP6 models could be due to an overestimate in aerosol radiative forcing during the period (Andrews et al., 2020; Dittus et al., 2020; Flynn and Mauritsen, 2020).

There have also been studies on regional climate using the CMIP6 models. For example, Khadka et al. (2021) used model data from CMIP5 and CMIP6 to evaluate summer rainfall in Southeast Asia. They found CMIP6 models to be superior to CMIP5 ones in simulating rainfall and large-scale circulation, and attributed it to CMIP6 models' higher spatial resolutions, increased number of vertical levels, and improved atmospheric and land surface parameterizations. They also reported that CMIP6 models are better at representing the annual cycle of rainfall but many still show dry biases like their predecessors. Many of the climate models from both CMIPs were reported to show a shorter rainy season due to late onset and early retreat. In another relevant study Ge et al. (2021) used outputs from 15 CMIP6 GCMs to estimate projected changes in precipitation extremes for SEA at the end of the 21st century and reported that the projected precipitation extremes increase significantly over the Indochina Peninsula and the Maritime Continent.

The IPCC AR6 further reports with medium confidence that CMIP5 and CMIP6 models continue to overestimate observed warming in the upper tropical troposphere over the 1979-2014 period by at least 0.1°C per decade, partly because of an overestimation of the tropical SST trends during this period.

Kim et al. (2020) evaluated CMIP6 models for their performance in simulating the climate extreme indices defined by the Expert Team on Climate Change Detection and Indices (ETCCDI) and reported that the CMIP6 models generally capture the observed global and regional patterns of temperature extremes with limited improvements compared to the CMIP5 models. They also reported that the CMIP6 model skills for the precipitation intensity and frequency indices are broadly comparable to those of CMIP5 models, but with an improvement in precipitation intensity amplitudes.

Fiedler et al. (2020) evaluated the simulation of MJO in CMIP6 models by calculating the ratio of the eastward-propagating spectral power of tropical precipitation to that of its westward-propagating counterpart summed up over the MJO characteristic wavenumbers one to three and periods of 20–100 days for the November to April season between 10oS and 10oN (a quantity often used as a measure for the MJO). It was found that while for observations this ratio was found to be in the range of 3.2 to 3.4 for CMIP6 multi model mean it was found to be around 2.2. While this is better than that in CMIP6, there is scope for further improvement in future CMIPs. In the same paper they also evaluated ENSO-rainfall teleconnections in the CMIP6 models by using the method from Power et al. (2013) by computing the empirical orthogonal function (EOF) of SST

means for June–December within 15oS–15oN, 140oE–100oW, based on detrended and filtered SST time series, and found that there are two clear regions with systematic biases in precipitation associated with El Niño events, (i) too-strong positive anomaly around the Maritime Continent indicating a westward displaced precipitation maximum during El Niño events, and (ii) too pronounced double ITCZ.

The IPCC AR6 Atlas provides only the large-scale information, and higher resolution information still needs to be generated by means of downscaling. Most of the CMIP6 models that have contributed to the WG-I report do not have Singapore as an island due to coarse resolution, and either represent it as a part of the Malay peninsula or show it as an ocean point. In order to make physical climate change projections on regional scales and also for making the global model data usable by the vulnerability and impacts assessment community, the coarse resolution global model data needs to be downscaled to higher resolutions. As was the case with CMIP5, CMIP6 also provides 6-hourly fields of model variables that can be further used to carry out dynamical downscaling to generate more reliable high resolution climate change projections at a regional level. It is imperative to thoroughly evaluate the historical simulations against observations and reanalysis to have confidence in the future large-scale climate change projections, and also for sub-selection of the models for downscaling.

Dynamically downscaled projections are produced in a coordinated way under the Coordinated Regional Climate Downscaling Experiment (CORDEX), a programme under the auspices of the World Climate Research Programme (Giorgi et al., 2009). During the last few years, a set of downscaled RCMs projections for the Southeast Asia domain has become available under the Coordinated Regional Climate Downscaling Experiment – Southeast Asia (CORDEX-SEA) (Juneng et al., 2016; Ngo-Duc et al., 2017; Supari et al., 2020; Tangang et al., 2018, 2020), and is used by SEA countries for their national climate change assessments and adaptation planning.

As a part of the Third National Climate Change Study for Singapore (V3) the Centre for Climate Research Singapore (CCRS) has dynamically downscaled 6 CMIP6 GCMs over Southeast Asia to 8 km resolution, and 5 of them were further downscaled over the western Maritime Continent to 2 km resolution for the historical period (1955-2014) and future (2015-2100) for 3 Shared Socioeconomic Pathways (SSPs) used in the IPCC AR6, namely, SSP1-2.6, SSP2-4.5 and SSP5-8.5. The dynamical downscaling domain is discussed in Chapter 2, and SINGV-RCM is discussed in Chapter 6 of this report.

There is no universally accepted methodology on how to select a subset of GCMs for downscaling, but in order to be consistent with the practice of the dynamical downscaling community, we follow a methodology in-line with the CORDEX experiment design protocol standard described in Section 5.2.4. The data and methods used in this work are described in Section 5.2. The evaluation of CMIP6 GCMs and the process of sub-selection is presented in Section 5.3, followed by discussion and conclusions presented in Section 5.4.

5.2 Data and Methods

In this section we present the various datasets used (observations, reanalysis and CMIP6 model outputs), the different metrics used for evaluation (root mean squared error, pattern correlation coefficient, etc.), the sub-setting criteria used, and the domain of evaluation such that it is relevant for our purpose of dynamical downscaling.

5.2.1 CMIP6 Model Data

Model outputs from historical simulations of 49 CMIP6 GCMs were used in our analysis. For some of the variables data from all 49 GCMs were not available so we used whatever was available during the time of analysis. Information on the GCMs, including their name, modelling centre, nominal grid resolution and ensemble member used in analysis have been presented in Table 5.1. The variables include 2m air temperature, surface temperature, rainfall, 2m specific humidity, winds and mean sea level pressure. We have used the period 1995-2014 for most of the evaluations.

Table 5.1: List of CMIP6 GCMs, modelling centre, nominal grid resolution and ensemble member. The dark green colour highlights models which had 6-hourly data available at the time of the downscaling.

Sl. No.	Model Name	Institution	Country	Nominal Resolution	Ensemble member
1	ACCESS-CM2	CSIRO-ARCCSS-BoM	Australia	250 km	/r4i1p1f1
2	ACCESS-ESM1-5	CSIRO	Australia	250 km	r1i1p1f1
3	AWI-CM-1-1-MR	AWI	Germany	100 km	r1i1p1f1
4	BCC-CSM2-MR	BCC	China	100 km	r1i1p1f1
5	BCC-ESM1	BCC	China	250 km	r1i1p1f1
6	CAMS-CSM1-0	CAMS	USA	100 km	r1i1p1f1
7	CESM2	NCAR	USA	100 km	r1i1p1f1
8	CESM2-FV2	NCAR	USA	250 km	r1i1p1f1
9	CESM2-WACCM	NCAR	USA	100 km	r1i1p1f1
10	CESM2-WACCM-FV2	NCAR	USA	100 km	r1i1p1f1
11	CIESM	THU	China	100 km	r1i1p1f1
12	CNRM-CM6-1	CNRM-CERFACS	France	250 km	r1i1p1f2
13	CNRM-CM6-1-HR	CNRM-CERFACS	France	50 km	r1i1p1f2
14	CNRM-ESM2-1	CNRM-CERFACS	France	250 km	r1i1p1f2
15	CanESM5	CCCma	Canada	500 km	r1i1p1f1
16	CanESM5-CanOE	CCCma	Canada	500 km	r1i1p2f1
17	E3SM-1-0	DOE E3SM-Project	USA	100 km	r1i1p1f1
18	E3SM-1-1	DOE E3SM-Project	USA	100 km	r1i1p1f1
19	E3SM-1-1-ECA	DOE E3SM-Project	USA	100 km	r1i1p1f1
20	EC-Earth3	EC-Earth-Consortium	Europe	100 km	r1i1p1f1
21	EC-Earth3-Veg	EC-Earth-Consortium	Europe	100 km	r1i1p1f1
22	FGOALS-f3-L	CAS	China	100 km	r1i1p1f1
23	FGOALS-g3	CAS	China	250 km	r1i1p1f1
24	FIO-ESM-2-0	FIO-QLNM	China	100 km	r1i1p1f1
25	GFDL-CM4	NOAA-GFDL	USA	100 km	r1i1p1f1
26	GFDL-ESM4	NOAA-GFDL	USA	100 km	r1i1p1f1
27	GISS-E2-1-G	NASA-GISS	USA	250 km	r1i1p1f1
28	GISS-E2-1-G-CC	NASA-GISS	USA	250 km	r1i1p1f1
29	GISS-E2-1-H	NASA-GISS	USA	250 km	r1i1p1f1
30	HadGEM3-GC31-LL	MOHC	UK	250 km	r1i1p1f3
31	HadGEM3-GC31-MM	MOHC	UK	100 km	r1i1p1f3
32	INM-CM4-8	INM	Russia	100 km	r1i1p1f1
33	INM-CM5-0	INM	Russia	100 km	r1i1p1f1
34	IPSL-CM6A-LR	IPSL	France	250 km	r1i1p1f1
35	KACE-1-0-G	NIMS-KMA	South Korea	250 km	r1i1p1f1
36	MCM-UA-1-0	UA	USA	250 km	r1i1p1f1
37	MIROC-ES2L	MIROC	Japan	500 km	r1i1p1f2
38	MIROC6	MIROC	Japan	250 km	r1i1p1f1
39	MPI-ESM-1-2-HAM	HAMMOZ-Consortium	Germany	250 km	r1i1p1f1
40	MPI-ESM1-2-HR	MPI-M	Germany	100 km	r1i1p1f1
41	MPI-ESM1-2-LR	MPI-M	Germany	250 km	r1i1p1f1
42	MRI-ESM2-0	MRI	Japan	100 km	r1i1p1f1
43	NESM3	NUIST	China	250 km	r1i1p1f1
44	NorCPM1	NCC	Norway	250 km	r1i1p1f1
45	NorESM2-LM	NCC	Norway	250 km	r1i1p1f1
46	NorESM2-MM	NCC	Norway	100 km	r1i1p1f1
47	SAM0-UNICON	SNU	South Korea	100 km	r1i1p1f1
48	TaiESM1	AS-RCEC	Taiwan	100 km	r1i1p1f1
49	UKESM1-0-LL	MOHC	UK	250 km	r1i1p1f2

5.2.2 Observations and Reanalysis

Multiple observational and reanalysis datasets have been used for evaluation. See Table 5.2 for details. We have used ensemble means of observations/reanalysis where feasible as our baseline to compute model biases, to address observational/reanalysis uncertainty.

Table 5.2: List of gridded observational (blue) and reanalysis data sets (green) used for evaluation in this chapter (all the data was regridded to 1.5°x1.5°, monthly, below shows the original grids), their climate fields used, and reference. The abbreviation pr refers to precipitation; TAS: surface air temperature; PSL: mean sea level pressure; SST: sea surface temperature; HUSS: specific humidity.

NAME	FIELDS (resol./freq.)	REFERENCES
HadISST v1	SST (1°x1°, monthly)	Rayner et al. 2003
COBE v2	SST (1°x1°, monthly)	Hirahara et al. 2014
OISST v2	SST (0.25°x0.25°, monthly)	Reynolds et al. 2007
ERSST v5	SST (2°x2°, monthly)	Huang et al. 2017
HURRELL	SST (1°x1°, monthly)	Hurrell et al. 2008
HadCRUT4	TAS (5°x5°, monthly)	Morice et al. 2012
BEST	TAS (1°x1°, monthly)	Rohde and Hausfather, 2020
FROGs	PR (1°x1°, daily)	Roca et al. 2019
IMERG V06	PR (0.1°x0.1°, 30 mins)	Huffman et al., 2019
GSMAP	PR (0.1°x0.1°, hourly)	Okamoto et al. 2005
TRMM 3B42	PR (0.25°x0.25°, 3 hours)	Huffman et al., 2007
PERSIANN_CDR	PR (0.25°x0.25°, sub-daily)	Ashouri et al., 2015
CMORPH_v1	PR (0.25°x0.25°, 3 hours)	Xie et al., 2017
GPCP	PR (1°x1°, daily)	Adler et al. 2003
ERA5 reanalysis	SST, TAS, HUSS, PSL, WINDS (0.25°x0.25°, hourly)	Hersbach et al. 2020
MERRA2 reanalysis	SST, TAS, HUSS, PSL, WINDS (0.5° x 0.625°, daily)	Gelaro et al. 2017
JRA55 reanalysis	SST, TAS, HUSS, PSL, WINDS (0.56°x0.56°, sub-daily, monthly)	Kobayashi et al. 2015

5.2.3 Metrics

Various statistical measures such as pattern correlation coefficient (PCC), mean absolute error (MSE), and root mean square error (RMSE) have been used to assess the performance of the models against observations and reanalysis. In addition, advanced metrics such as the Taylor diagram have also been used to assess the performance of the models.

5.2.4 Sub-setting of CMIP6 GCMs

In order to carry out sub-selection we follow standard practices suggested by the coordinated regional climate downscaling experiment (CORDEX; e.g. Gutowski et al. 2016). Thus, the sub-selected GCMs should: (1) span the range of GCM projections of temperature and precipitation over SEA, (2) perform satisfactorily in the historical climate, (3) span the range of model diversity in terms of genealogy (e.g., Knutti et al. 2013), and (4) have 6-hourly lateral boundary conditions (LBCs) available to drive the regional climate model. In addition to the aforementioned criteria, we also make use of expert judgement to discard models that are unable to simulate important aspects of regional climate over SEA.

5.2.5 Domain

Our domain of analysis focuses mostly on SEA, but for some of the tropical processes of interest included in tier-II of the analysis we have used larger domains. For example, for ENSO and cold-tongue bias analysis we have used the entire tropical Pacific domain. Figure 5.1 shows the 8 km and 2 km downscaling domains used in the V3 study. The D1 domain (8 km resolution) covers almost the whole of SEA and is slightly larger than

the CORDEX-SEA domain, whereas, the D2 domain (2 km resolution) covers Singapore and the western Maritime Continent. We use a one-way offline nesting, and the lateral boundary conditions for the 2 km model come from the 8 km downscaled data. Since the lateral and lower boundary conditions to drive the 8 km downscaling are obtained directly from the CMIP6 GCMs, our evaluation primarily focuses on the 8 km domain.

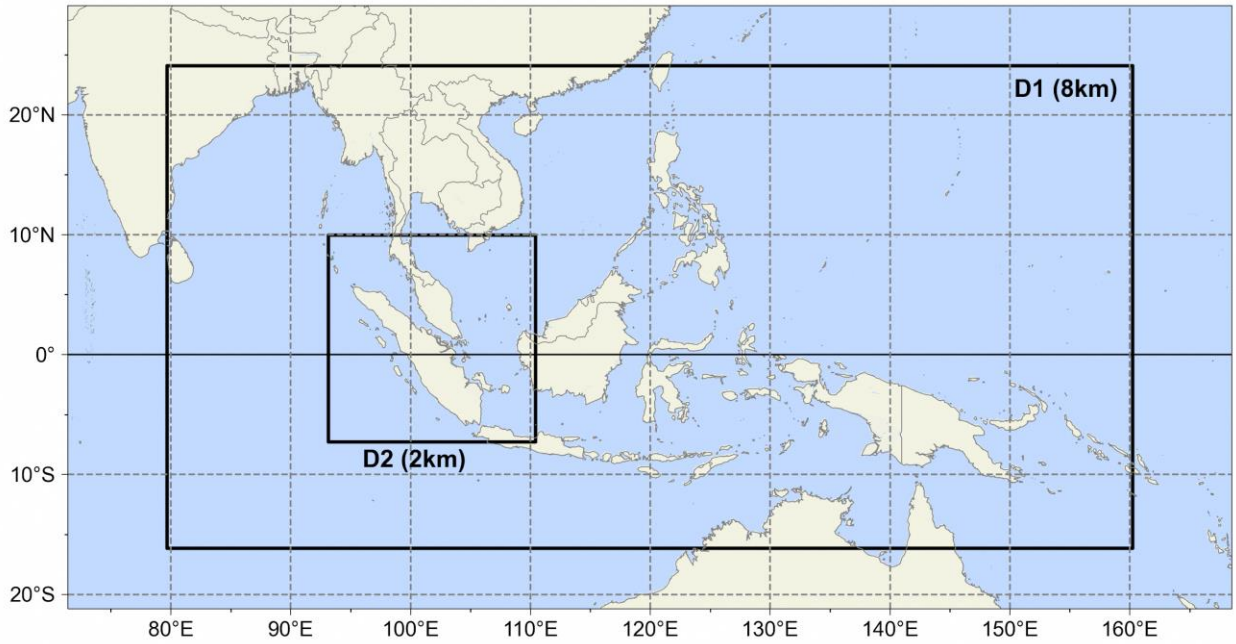

Figure 5.1: Dynamical downscaling domains for Singapore's Third National Climate Change Study at 8 km and 2 km resolutions.

5.3 Evaluation of Key Climate Variables

In this section we present the evaluation of key climate variables, namely, temperature, rainfall, winds, humidity and mean sea level pressure from the CMIP6 GCMs with an objective to identify the GCMs that show consistently poor performance and hence may not be considered fit for downscaling. The resolution used for multi-model mean for the GCMs is 1.5º, although not the lowest model resolution, it is the resolution fits for majority of the models. Thus, all the variables are conservatively re-gridded to 1.5º. The observational datasets are mostly 1º degree then all re-gridded to 1.5º to be able to compare to the model outputs.

5.3.1 Temperature

Figure 5.2 shows the climatological annual mean surface air temperature (tas) in observations (and reanalysis) and CMIP6 GCMs. Overall, the models perform well on annual timescales with low biases (white colour; biases in the range of +/- 0.5C) over almost half of the domain. For example, the biases are quite low over the tropical Indian Ocean. However, there are some notable biases which can be seen from Figs. 5.2e and f. Figure 5.2e shows (i) large positive biases over the Southern Ocean and east Pacific, (ii) negative biases over western and central tropical Pacific, (iii) negative bias over North Atlantic, and (iv) negative bias over Indochina. Figure 5.2f shows that the bias over large parts of the Maritime Continent is within +/- 0.5C, with exceptions such as Indochina and tropical western Pacific which show negative biases.

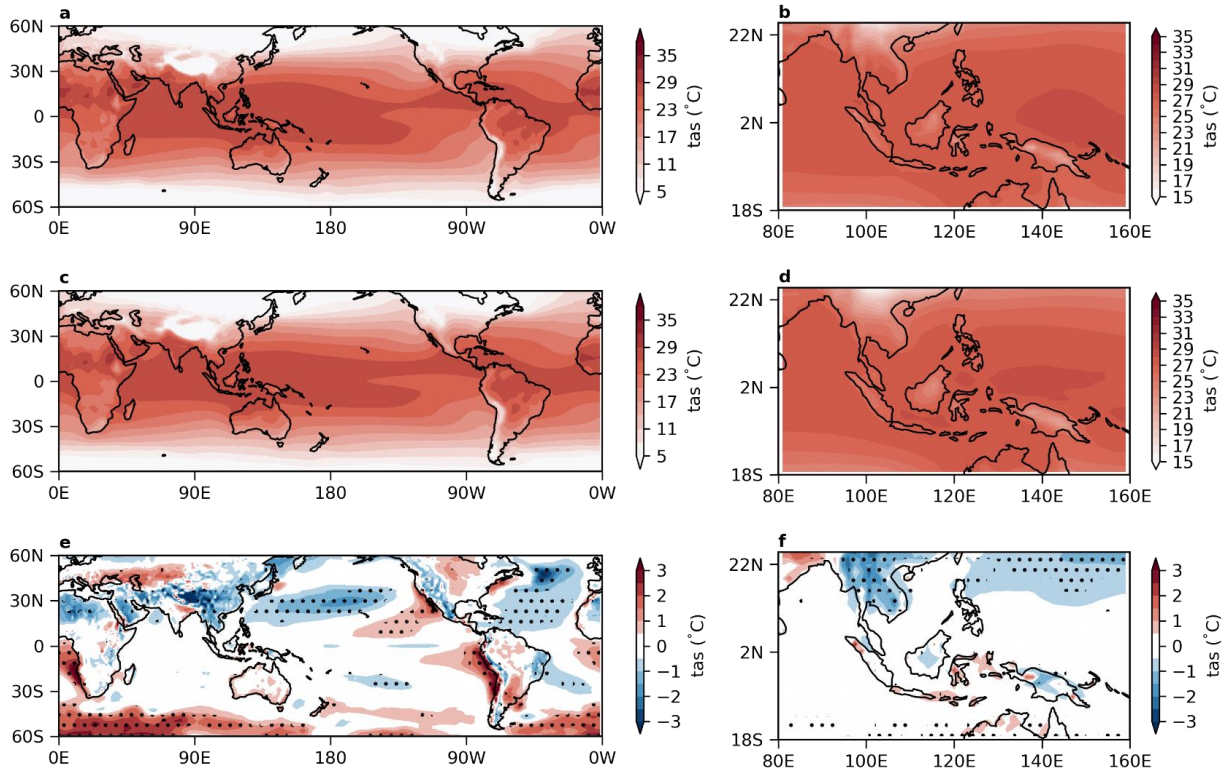

Figure 5.2: 1995-2014 mean surface air temperature (tas) in observation (a,b) and models (c,d). a. mean of five observational and reanalysis datasets (BEST, ERA5, HADCRUT4, JRA55, and MERRA2) for the 60N-60S domain. b. similar to a, but for the SEA domain. c. multimodel mean of tas from 47 CMIP6 models for the 60N-60S domain. d. similar to c, but for the SEA domain. e. model bias (multimodel mean from 47 models minus the observational mean). Hatched areas indicate the agreement by 70% of models on the sign of bias. f. similar to e, but for the SEA domain.

Figure 5.3 shows the distribution of model simulated tas values along with their RMSE and PCC for the global and SEA domains and for the annual mean and all seasons. Figure 5.3a, b show that the median of the multimodal ensemble lies within the spread of the reanalysis for annual mean as well as for each season over both global and SEA domains. The 25-75 percentile range of tas in models spans the reanalysis uncertainty range for all seasons and both domains. Figure 5.3c, d show that the median RMSE values are highest in DJF over both domains as compared to annual mean and other seasons. Given that the mean tas for DJF is already lower as compared to other seasons, higher RMSE values would mean even higher percentage errors. Figure 5.3e, f shows that the median PCC values are much higher over the global domain (~0.99), whereas it is somewhat lower over the SEA domain. Notably, the DJF PCC values are higher, especially over SEA.

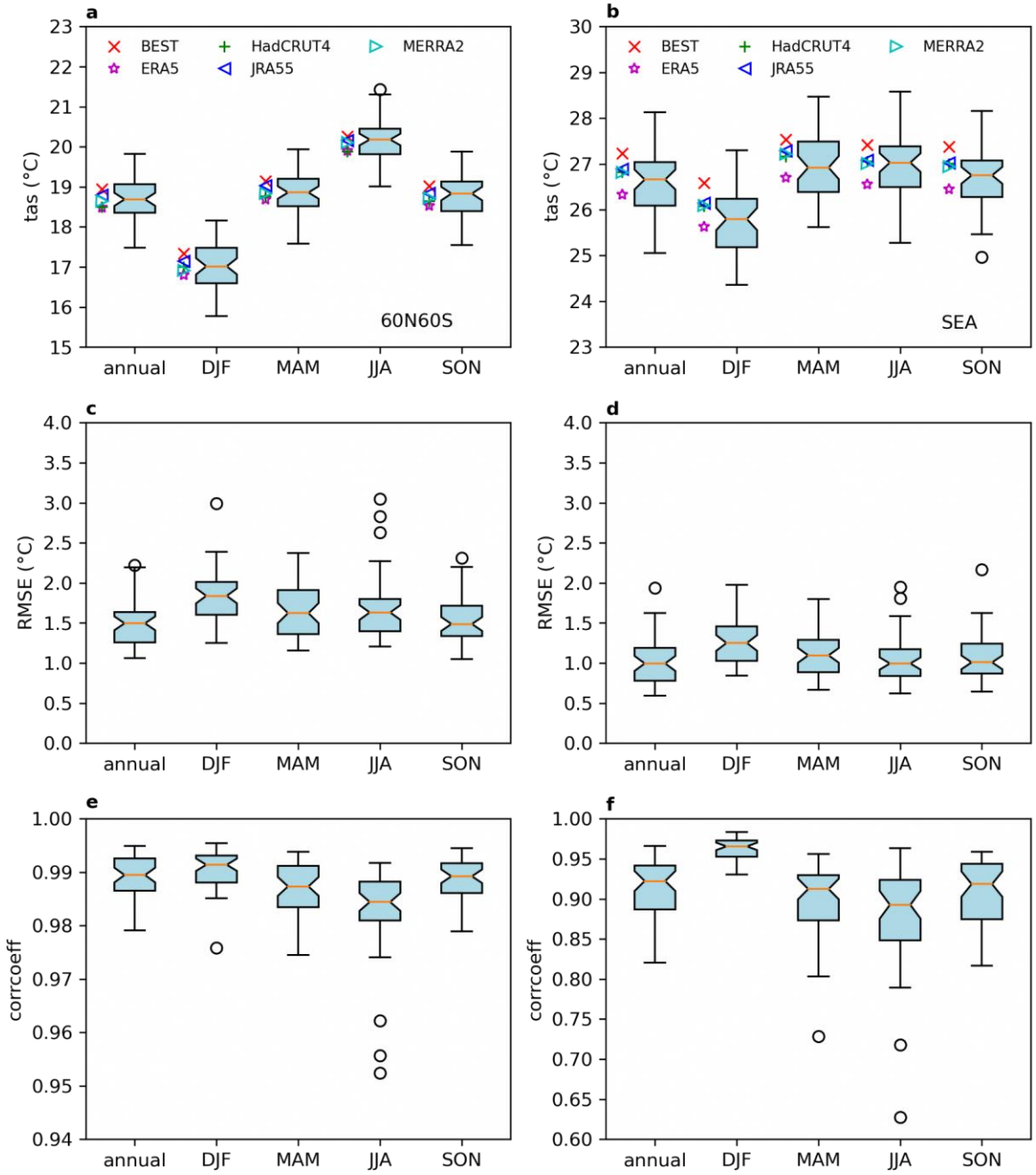

Figure 5.3: 1995-2014 mean tas averaged over the 60N-60S domain (a) and the SEA (b) in five observational and reanalysis datasets and 47 CMIP6 models. c. RMSE of models for the annual and seasonal tas in the 60N60S. d. similar to c, but for the SEA. e. PCC of models for the annual and seasonal tas in the 60N60S. f. similar to e, but for the SEA. The orange lines represent the median. The lower hinge is the Q1 quartile (25th), and the upper hinge is the Q3 quartile (75th). The upper and lower bars are based on 1.5 times the interquartile range (IQR) value. The outliers are shown in the open circles.

Figure 5.4 shows the performance of the individual CMIP6 GCMs for the global (60oS to 60oN) and SEA domains assessed from their RMSE and PCC values. For the global domain, we find that the annual mean RMSE mostly lies between the range of 1oC to 2oC, with around 5 models exceeding 2oC. The seasonal means also show a similar behaviour. It is to be noted that we

exclude the poles because we noted much larger biases over the polar region that may not be directly relevant to our purpose of sub-selection and at the same time masks the performance of the GCMs in the mid- and low-latitudes because of their lower values as compared to the higher latitudes. RMSE over SEA domain (Fig. 5.4b) mostly lies between around 0.7oC to 2oC, which was counter-intuitive since we were expecting regional biases to be larger than the global biases, but the regional biases over different regions can be higher or lower than the global mean, and it was good to see that the CMIP6 models have lower biases over our domain of interest. It is to be noted that many of the models show higher biases in DJF compared to other seasons and annual mean. The bottom five models based on annual mean RMSE are NorCPM1, BCC-ESM1, CNRM-CM6-1, BCC-CSM2-MR, and CNRM-CM6-1-HR.

The PCCs are shown in Figure 5.4c, d, for the global and SEA domains, respectively. The PCCs are generally quite high over the global domain with values greater than around 0.94 for the annual mean as well as all seasons. However, the PCCs over the SEA domain, in general, seem to be lower than the global, with values as low as around 0.65 for the JJA season. In general, DJF seems to have the highest PCCs, whereas JJA seems to have the lowest PCCs. Note that while the PCCs are generally higher in DJF, the RMSEs are also higher, as seen above. The bottom five models based on annual mean PCCs over the SEA domain are INM-CM4-8, NorCPM1, MCM-UA-1-0, GISS-E2-1-H, and MIROC-ES2L.

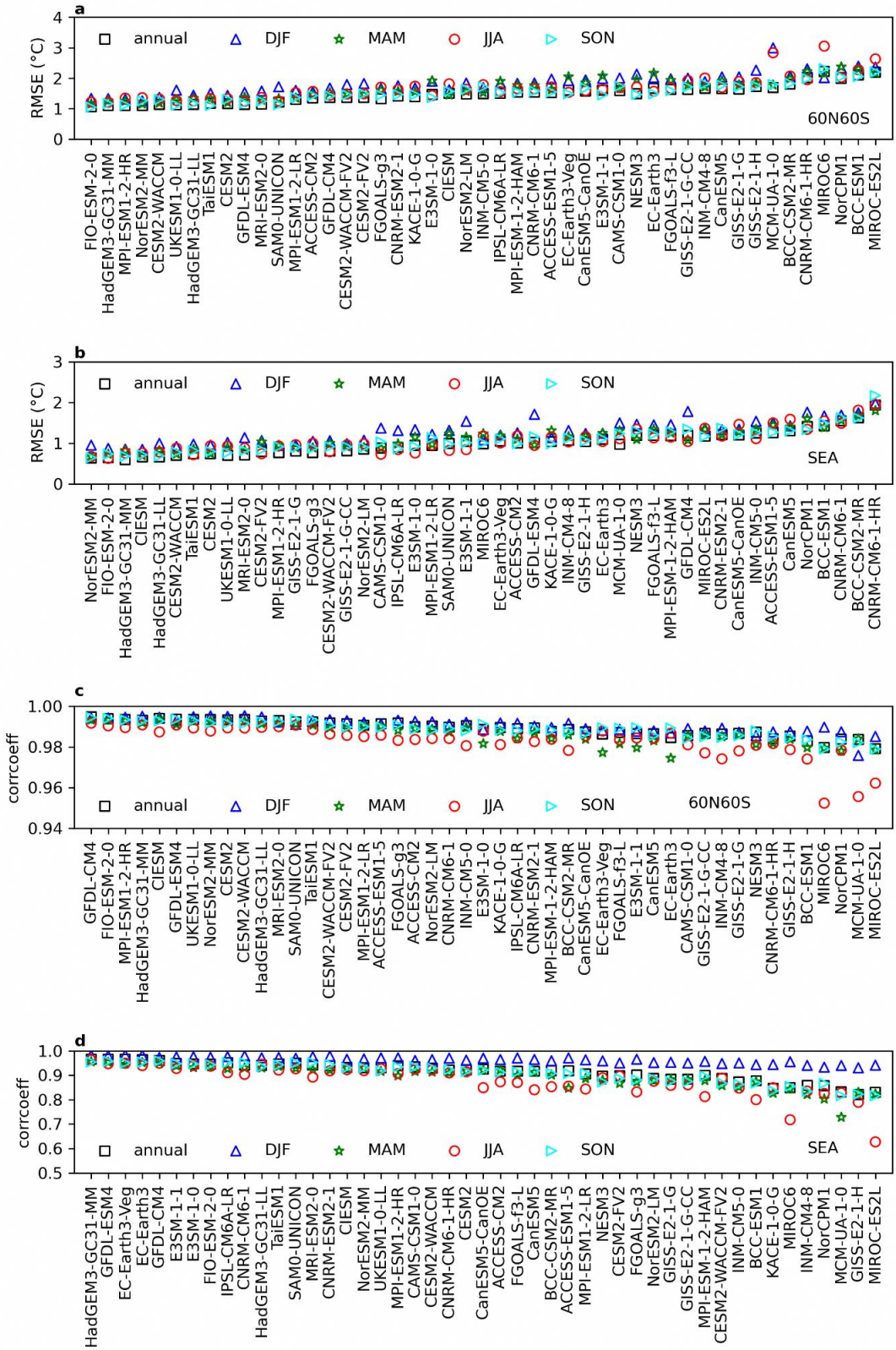

Figure 5.4: Performance of CMIP6 models as to RMSE for the annual and seasonal tas over the 60N60S (a) and SEA (b). Performance of CMIP6 models as to PCC for tas over the 60N60S (c) and SEA (d).

5.3.2 Rainfall

Similar analysis as presented above for near-surface air temperature is then carried out for rainfall and presented in Figures 5.5 to 5.7. Figure 5.5 shows the annual mean precipitation for the global and SEA domains and the corresponding biases based on multi-model means. From Figures 5.5a and 5.5c it can be seen that overall the CMIP6 GCMs perform well in simulating the large scale pattern and magnitude of rainfall, although there are some biases that can be more clearly seen in panels e and f of the figure. For example, even from the absolute values we can see the well-known double ITCZ bias over the tropical Pacific which has been present in previous generations of CMIP. From Figure 5.5e it can be seen that there are robust biases (based on 70% model agreement) over the tropical Pacific, tropical Atlantic, and western equatorial Indian ocean. Zooming into the SEA domain, we find positive biases over the South China Sea and over east of Borneo. In contrast, we see a large negative bias over the northern Bay of Bengal. Similar to the annual mean rainfall in Figure 5.5, JJA season rainfall in FigureA5.1 and the DJF season rainfall in Figure A5.2 also show consistent understanding of the evaluations.

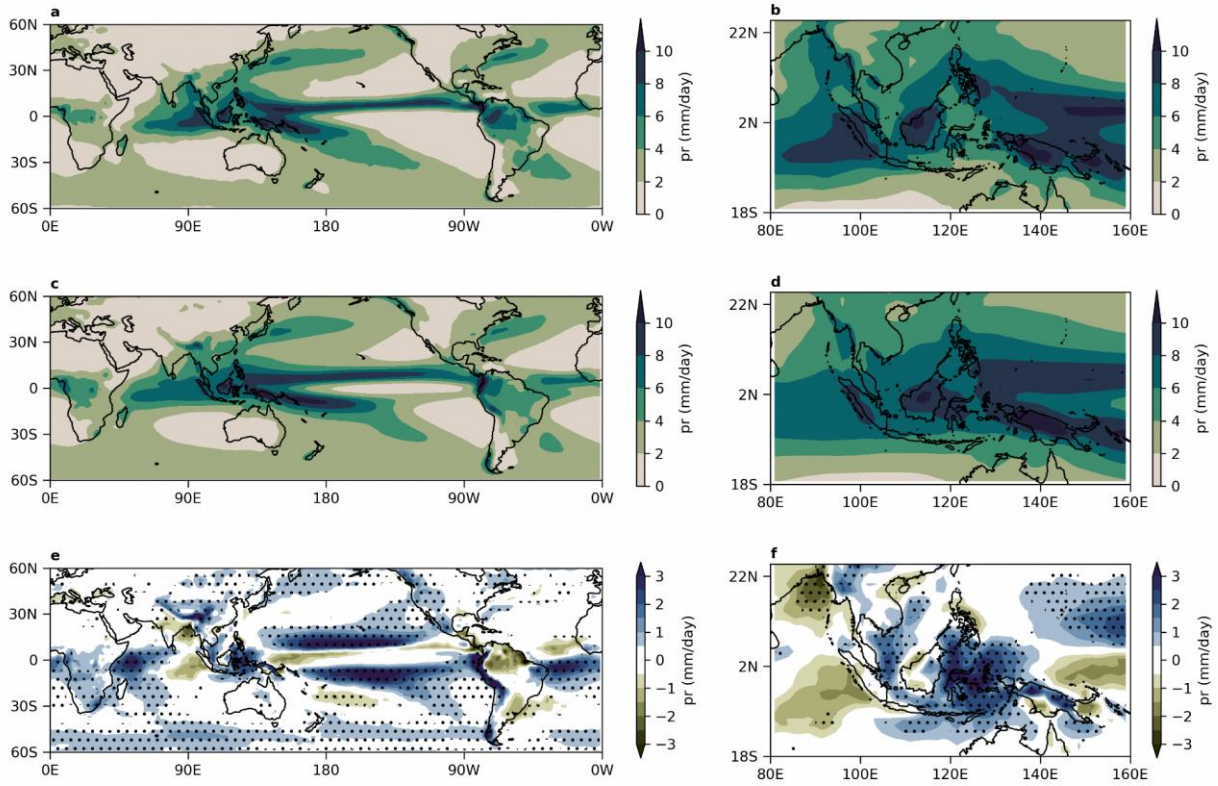

Figure 5.5: 1995-2014 mean precipitation (pr) in observation (a, b) and models (c, d). a. FROGS datasets for the 60N-60S domain. b. similar to a, but for the SEA domain. c. multi-model mean of pr from 48 CMIP6 models for the 60N-60S domain. d. similar to c, but for the SEA domain. e. model bias (e.g., multi-model mean from 48 models minus the observational mean). Stippled areas indicate the agreement by 70% of models. f. similar to e, but for the SEA domain.

Figure 5.6 shows the inter-model spread of the absolute values of precipitation, RMSE, and PCC over the global and SEA domains. From Figure 5.6a we see that the observed mean for the global domain is around 2.8mm/day, for annual as well as for various seasons with small seasonal variations. The CMIP6 GCMs, overall, overestimate the rainfall on seasonal as well as annual timescale scales with the median of the inter-model spread showing a value of around 3.2 mm/day (an overestimate of around 14%). Notably, because of the overall overestimation in

the GCMs the one that is closest to observations is considered an outlier in the distribution. As expected, the observed annual and seasonal means are higher over the SEA domain with higher seasonal variations (JJA being the highest and MAM being the lowest). The CMIP6 GCMs are found to perform quite well over SEA with the median value of the multi-model distribution overestimating the observed values by up to 5% on annual as well as seasonal timescales.

From Figure 5.6c we find that the annual mean RMSE over the global domain is lower than the seasonal (as expected), and the values for MAM and JJA are slightly higher than other seasons. The RMSE values are relatively higher over the SEA domain on annual and seasonal timescales, with JJA showing the highest value and MAM showing the lowest, noting that these are also the wettest and driest seasons over the SEA domain, respectively (Figure 5.6d). For the global domain, the PCC values are generally high (0.8 to 0.9) for annual and all seasons except MAM (around 0.75), as seen from Figure 5e. Whereas, for the SEA domain, they are slightly lower (0.7 to 0.8), with DJF showing a somewhat higher PCC of around 0.83.

Figure 5.7 shows the annual and seasonal RMSE and PCC for the global and SEA domains for the individual models, with the best to worst shown from left to right, based on the annual values. For the global domain, the RMSE values are found to be higher in the JJA and MAM seasons, while for the SEA domain they are highest in JJA (Figure 5.7a, b). The bottom 5 models based on SEA annual performance using RMSE are MPI-ESM-1-2-HAM, INM-CM4-8, MCM-UA-1-0, FGOALS-g3, and IPSL-CM6A-LR.

For the global domain, MAM is found to have the lowest PCC, whereas, for the SEA domain the PCC values are higher during DJF and lower during JJA (Figure 5.7c, d). Overall, as expected, the PCC values are lower than global both on annual and seasonal timescales. The bottom 5 models based on annual rainfall PCC over the SEA domain are MPI-ESM-1-2-HAM, INM-CM5-0, MCM-UA-1-0, IPSL-CM6A-LR, and INM-CM4-8.

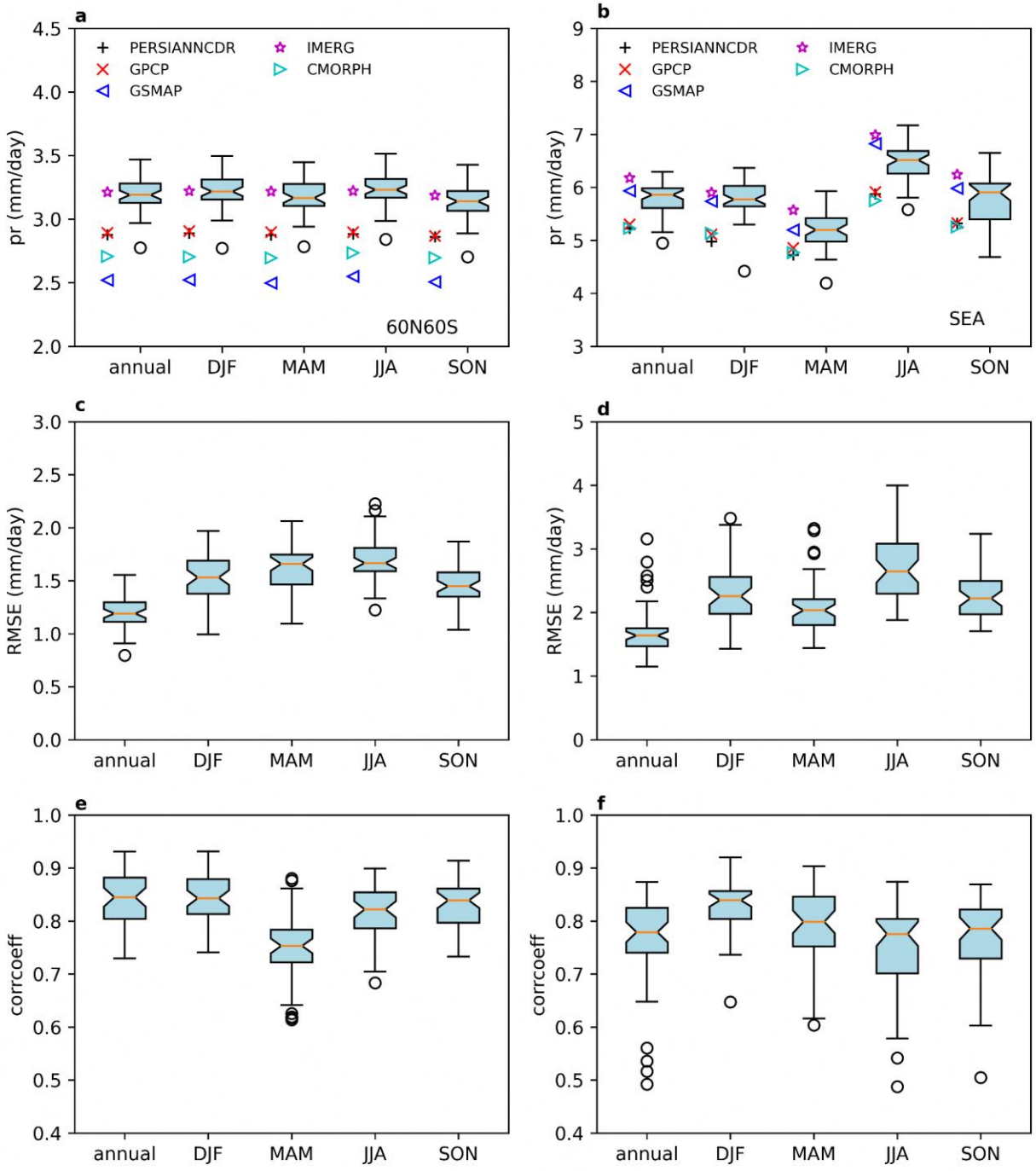

Figure 5.6: 1995-2014 mean pr averaged over the 60N-60S domain (a) and the SEA (b) in FROGS observational datasets (including PERSIANN-CDR, IMERG, GPCP, CMORPH, GSMAP) and 48 CMIP6 models. c. RMSE of models for the annual and seasonal pr in the 60N60S. d. similar to c, but for the SEA. e. PCC of models for the annual and seasonal pr in the 60N60S. f. similar to e, but for the SEA.

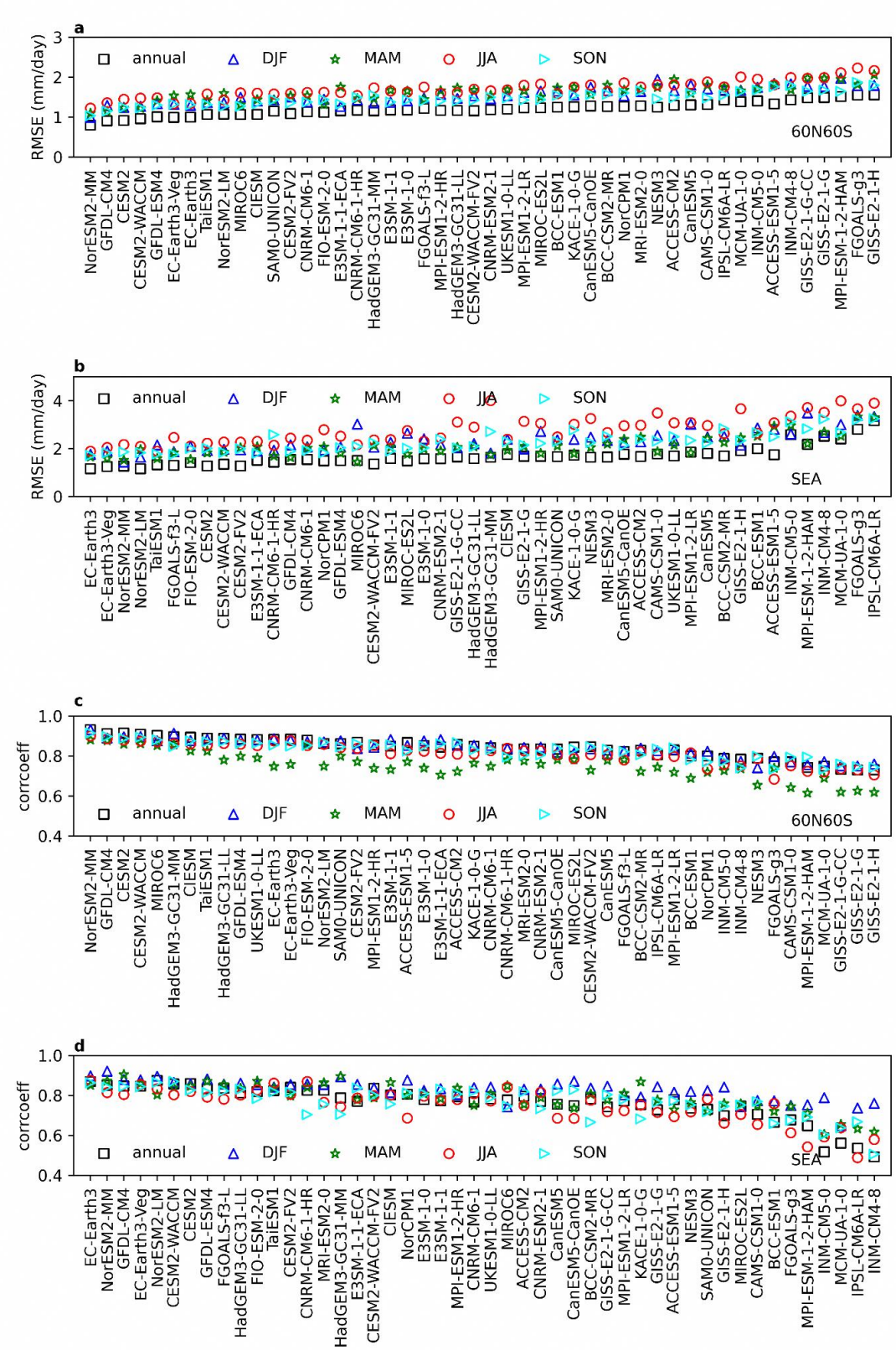

Figure 5.7: Performance of CMIP6 models as to RMSE for the annual and seasonal pr over the 60N60S (a) and SEA (b). Performance of CMIP6 models as to PCC for pr over the 60N60S (c) and SEA (d).

5.3.3 Mean Sea Level Pressure

In Figure 5.8 we compare the psl from 48 CMIP6 models to the ensemble-mean reanalysis (JRA-55, ERA5 and MERRA2) for the global and SEA domains.

The subtropical oceanic highs in reanalysis (Figure 5.8a) are well captured by the models (Figure 5.8c), as is the relatively low psl over SEA. Figures 5.8b, d show that the southwest to northeast spatial gradient in psl is also simulated in models. The sign of the bias is not systematic across models, and is generally higher outside SEA, with some of the highest values collocated with mountain ranges (e.g. Himalayas, Rockies, Andes). Over SEA, there is a high over Indochina and low around east Java and Sulawesi, alongside a corresponding low/high bias in tas. Nevertheless, biases in psl are relatively small over much of SEA.

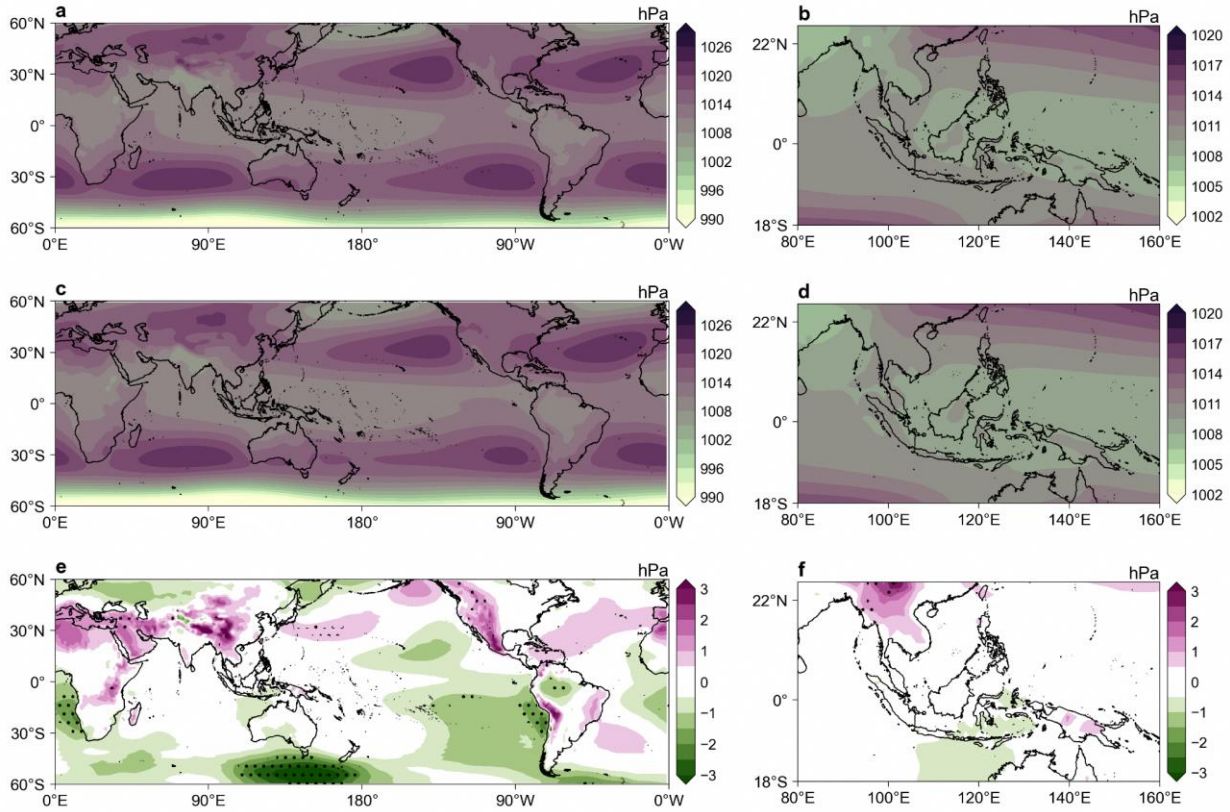

Figure 5.8: 1995-2014 mean sea level pressure (slp) in observation (a, b) and models (c, d). a. Mean of JRA-55, ERA5 and MERRA2 for the 60N-60S domain. b. Similar to a, but for the SEA domain. c. Multimodel mean of slp from 48 CMIP6 models for the 60N-60S domain. d. Similar to c, but for the SEA domain. e. Model bias (multimodal mean from 48 models minus the observational mean). Stippled areas indicate the agreement by 70% of models on the sign of bias. f. Similar to e, but for the SEA domain.

5.3.4 Humidity

Figure 5.9 shows the annual mean specific humidity (huss) from the ensemble mean reanalysis (JRA-55, ERA5 and MERRA2) for the global and SEA domains, the same from the CMIP6 multi-model means, and the corresponding biases. Overall, the large-scale pattern in huss is simulated well in CMIP6 GCMs, although there are regional biases which can be seen in Figure 5.9e, f. Over the global domain there is large negative bias over the Indian region, South America, and western and central North Pacific, whereas, there is positive bias over tropical eastern Pacific, east Atlantic near the west coast of Africa, and the southern oceans. Over the

SEA domain the biases are generally low, except for the dry bias over Indo-China, and southern equatorial Indian Ocean. Since the humidity field over the SEA domain is generally well simulated, we don't show the inter-model spread in RMSE and PCC, and the rankings of the individual models for this variable.

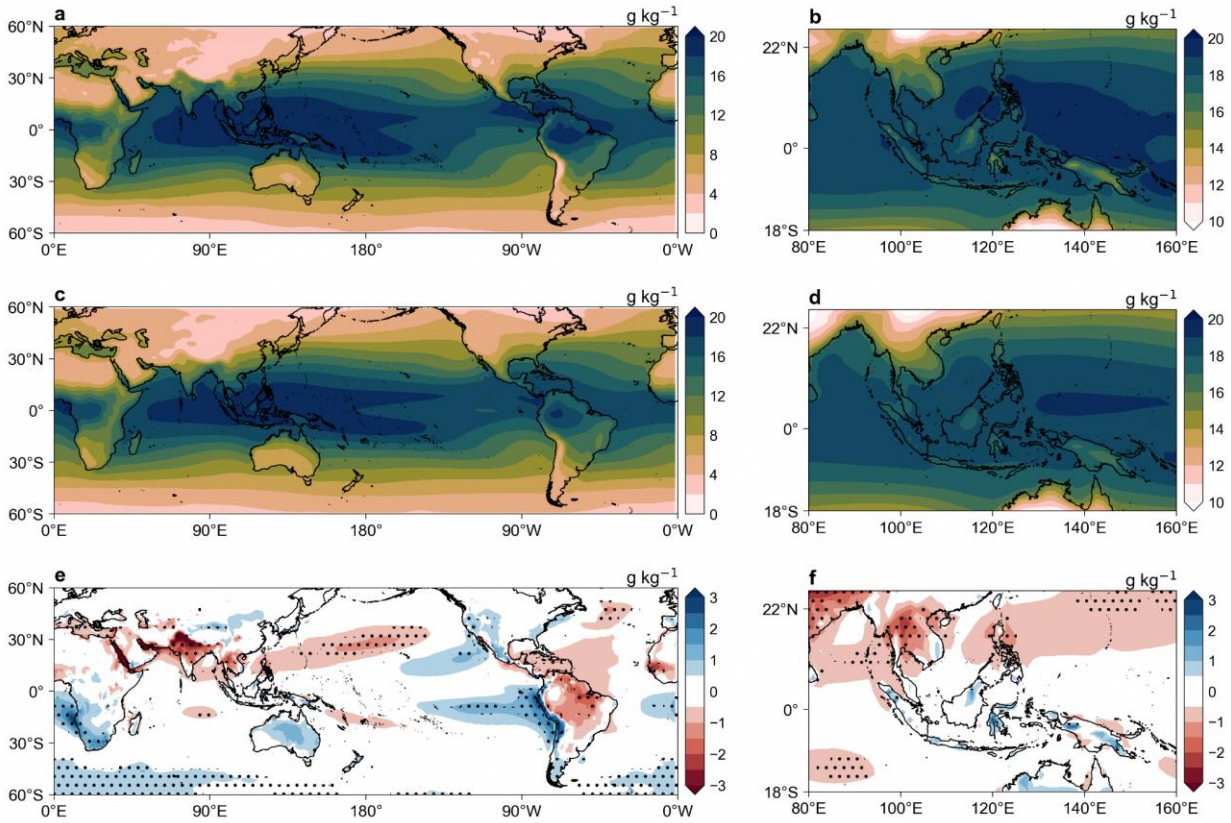

Figure 5.9: 1995-2014 annual mean specific humidity (huss) in reanalysis (a, b) and models (c, d). a. Mean of JRA-55, ERA5 and MERRA2 for the 60N-60S domain. b. Similar to a, but for the SEA domain. c. Multimodel mean of huss from 48 CMIP6 models for the 60N-60S domain. d. Similar to c, but for the SEA domain. e. Model bias (multimodal mean from 48 models minus the observational mean). Stippled areas indicate the agreement by 70% of models on the sign of bias. f. Similar to e, but for the SEA domain.

5.3.5 Winds

Next, we evaluate the 850hPa annual mean and seasonal winds over the global and SEA domains to check if there are any CMIP6 GCMs with unrealistic wind patterns, especially in regard to the monsoonal wind flow patterns.

The results of Tangang et al., (2019) indicate anomalously strong easterlies over Papua in JJA, as well as anomalous westerlies around the tip of Sumatra that extend to the Malay Peninsula. McSweeney et al., (2015) examined 39 CMIP5 GCMs and noted that models were generally able to simulate the Somali jet in terms of having the highest wind speeds near the core, as well as a predominantly westerly flow over India that turns south-westerly over the Bay of Bengal, then westerly over Indochina and turning southerly west of the Philippines.

A small number of models exhibited an unrealistic feature of the winds turning southerly west of continental Southeast Asia. Some models were also noted for a monsoon flow that was too weak (e.g. in the region of the Somali jet).

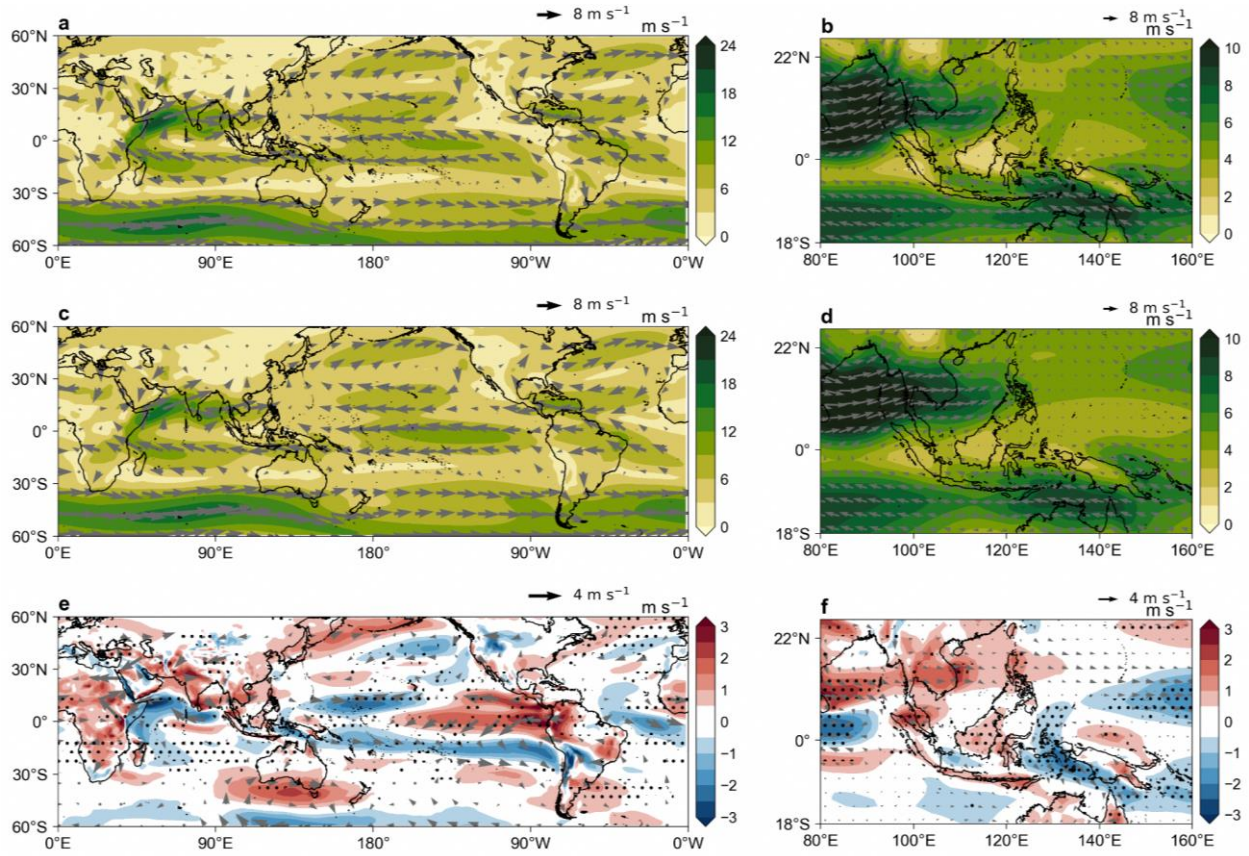

Figure 5.10: 1995-2014 annual mean 850hPa JJA winds in reanalysis (a, b) and models (c, d). a. Mean of JRA-55, ERA5 and MERRA2 for the 60N-60S domain. b. Similar to a, but for the SEA domain. c. Multimodel mean winds from 49 CMIP6 models for the 60N-60S domain. d. Similar to c, but for the SEA domain. e. Model bias (multimodel mean from 49 models minus the observational mean). Stippled areas indicate the agreement by 70% of models on the sign of bias. f. Similar to e, but for the SEA domain.

These observational features can be seen in Figure 5.10a, b. Figure 5.10c, d is broadly consistent with the notion that models are generally able to simulate the South-westerly monsoon. Models exhibit a diversity of responses with regard to the strength of the Somali Jet, being slightly weaker on average (Figure 5.10e). Here a positive bias in speed is shown to the north over the Arabian Sea and northern India.

Such characteristic anticyclonic bias is linked to the tendency for the westerly flow to extend too strongly over Southeast Asia into the South China Sea associated with an eastward shift and weakening of the Western North Pacific Subtropical High (WNPSH).

Over the East of India, there is a robust northward shift of wind speeds near Sri Lanka upstream of a robust increase in winds over the Malay Peninsula and Borneo and decrease in winds closer to New Guinea. Figure f indicates that the anomalously strong westerlies near the tip of Sumatra seen in the CMIP5 multi-model mean remains a common issue in CMIP6 GCMs. The representation of the monsoon in the individual models (not shown) is generally realistic.

A key feature of DJF circulation over the Maritime Continent is the turning of the northeasterly winds over the South China sea towards the Malay Peninsula, and its subsequent convergence with westerlies from the Indian ocean (McSweeney et al., 2015). This is generally captured by the multi-model mean (Figure 5.11a, d).

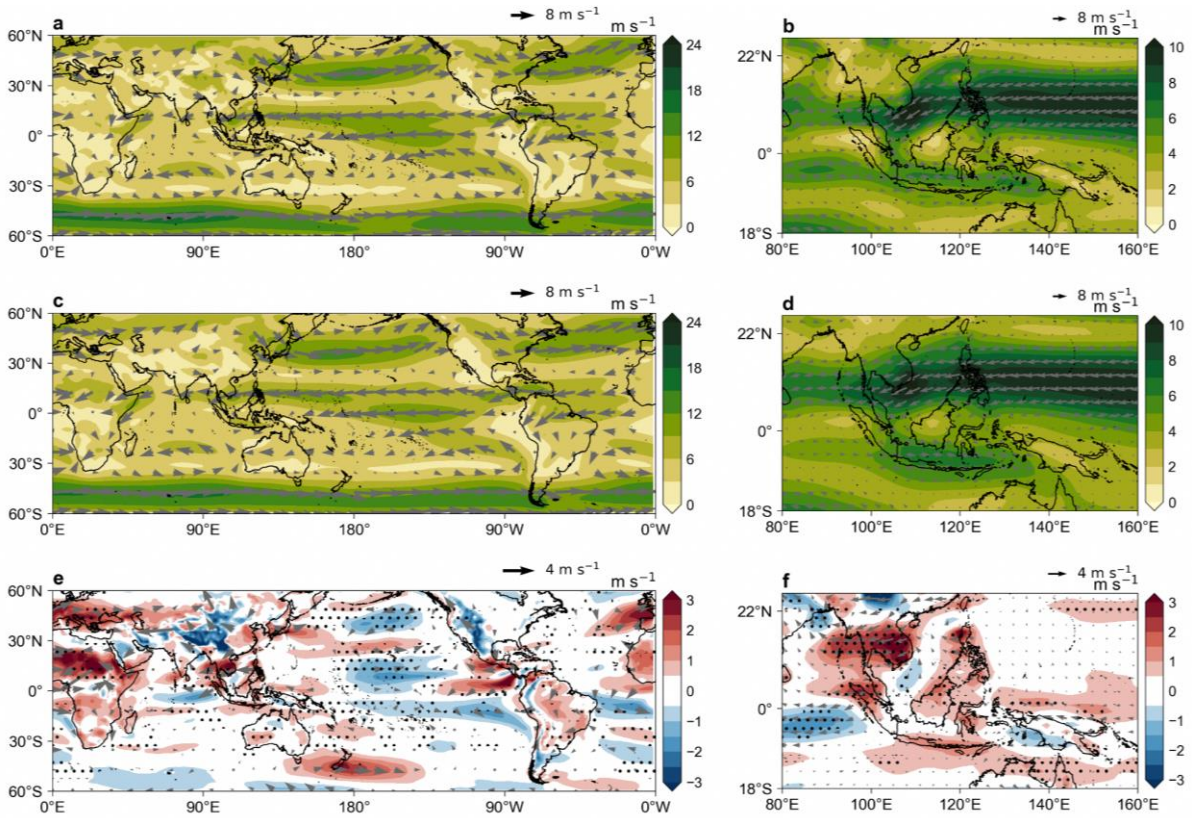

Figure 5.11: As in Fig. 5.10, but for DJF.

In their analysis of the ensemble mean of 11 CMIP5 GCMs, Tangang et al. (2019) noted an easterly component of wind that was too strong over Indochina in DJF, and anomalously strong easterlies over Papua. As for individual models, McSweeney et al., (2015) presented results from 38 CMIP5 GCMs and noted that some models had an anomalously strong easterly component, such that the flow was directed towards Vietnam rather than the Malay Peninsula.

Anomalously strong easterlies remain a robust bias in CMIP6 models (Figure 5.11d, f), together with anomalously strong outflows over the Indian Ocean (net reduction in wind speed).

Figure 5.12a, b shows the range of model ws850 values along with that from the reanalyses. Overall, we find that the models simulate ws850 satisfactorily. The median ws850 values are lower in SEA as compared to GLOB. However, in some cases, the RMSE of ws850 in SEA can exceed that of GLOB (Figure 5.12c, d). Pattern correlation of ws850 is generally quite high for GLOB but falls over SEA (below 0.6 in one case), as can be seen in Figure 5.12e, f.

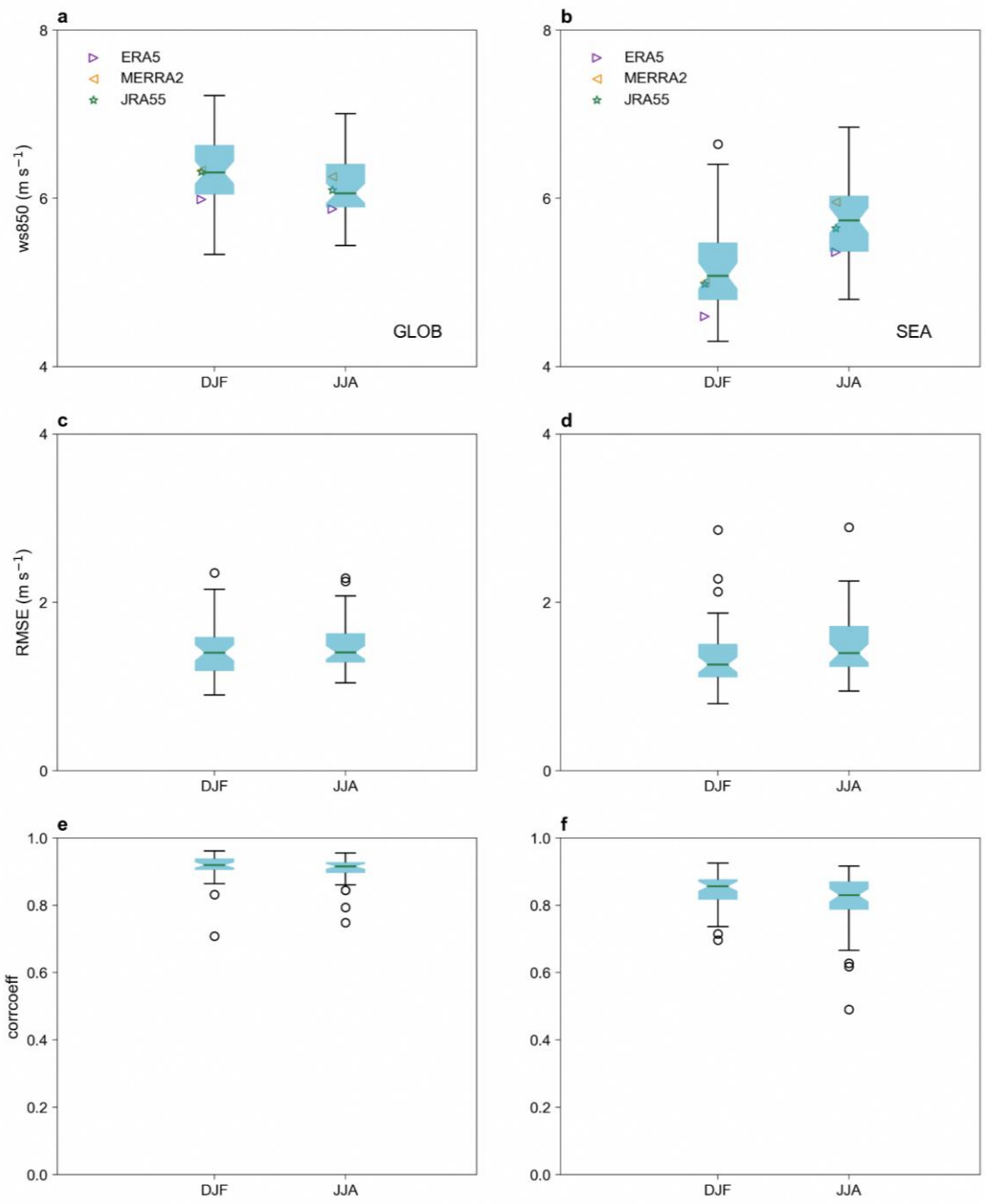

Figure 5.12: (a) Boxplot of wind speed at 850 hPa (ws850) over GLOB in CMIP6 models for DJF and JJA. Values for three reanalyses are shown with symbols. (c) Boxplots of RMSE of ws850 against values computed with the ensemble mean of the three reanalyses. (e) As in (c), but for pattern correlation. (b, d, f) as in (a, c, e), but over SEA.

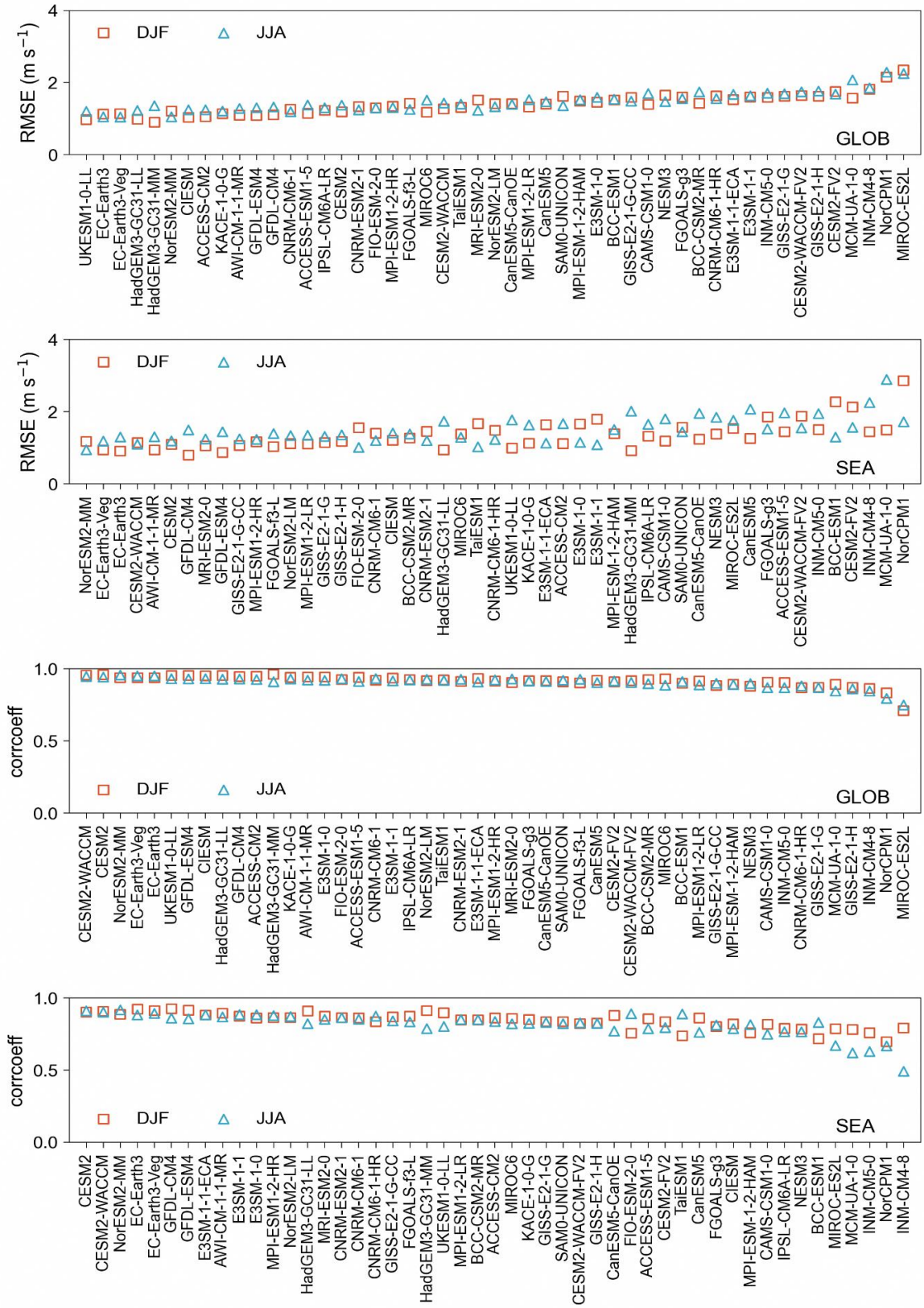

Figure 5.13: Model performance (better to worse) in ws850 as measured by RMSE over (a) GLOB and (b) SEA. (c-d). As in (a-b), but for pattern correlation.

Model simulations of ws850 are generally better over GLOB as compared to over SEA. Some notable outliers over SEA are NorCPM1, which has anomalously strong winds over Indochina and its nearby latitudinal region in DJF, and the INM models (INM-CM4-8 and INM-CM5-0), where the south-westerly monsoonal flow in JJA is weaker and/or angled too far north (above the South China Sea). Based on RMSE over the SEA domain for the 2 seasons, the bottom 5 models are BCC-ESM1, CESM2-FV2, INM-CM4-8, MCM-UA-1-0, and NorCPM1. Based on PCC the bottom 5 models are MIROC-ES2L, MCM-UA-1-0, INM-CM5-0, NorCPM1, and INM-CM4-8.

In summary, we find that, many of the CMIP6 GCMs are able to simulate the large-scale patterns of rainfall, temperature, winds, humidity and psl over the global and SEA domains, on annual and seasonal timescales. However, there are some biases in each of these variables that are regionally and seasonally dependent. Although many models are found to perform quite well, some are found to perform unsatisfactorily to an extent that we don't have enough confidence in them to consider for our dynamical downscaling. Some of the models that we have identified to discard are: INM-CM4-8, INM-CM5-0, NorCPM1, MCM-UA-1-0, and MIROC-ES2L.

5.4 Evaluation of Key Climate Processes

In this section we present the evaluation of key climate processes that are important drivers of weather and climate over Maritime Continent region, namely, monsoon, ENSO, IOD, equatorial Pacific cold tongue, northeast monsoon surge, and MJO from the CMIP6 GCMs with the same objective as the in section above, i.e. to identify the GCMs that show consistently poor performance and hence may not be considered fit for downscaling.

5.4.1 Monsoon

Monsoon rainfall, associated with changes in wind circulation and the north-south movement of the ITCZ dominates the seasonal variations of rainfall in the tropics. The easterlies in the southern hemisphere and westerlies in the northern hemisphere, along with the cross-equatorial flow over the western equatorial Indian ocean are notable features of the boreal summer monsoon (Figure 5.10a). Similarly, the corresponding wind circulation features can be seen from Figure 5.11a that are associated with the boreal winter monsoons. Monsoons have a key role in shaping the weather and climate of the MC domain. The MC domain is affected by the boreal summer monsoon (JJA; southwest monsoon) as well as the boreal winter monsoon (DJF; northeast monsoon).

Seasonal migration of ITCZ leads to climatological rainfall peaks during the monsoon season in Northern and Southern hemispheres. Figure 5.14 (top left) shows the observed migration of monsoon rainfall for the 1995-2014 period with NH peaks during JJAS and SH peaks in DJFM. Note the more persistent wet all year around in the equatorial (+/- 5 degrees) region. Also, the NH monsoon extends further north compared to the SH monsoon extension southward.

CMIP6 models on average simulate the seasonal migration of the ITCZ, but individual models can show significant systematic errors, such as shifting the monsoonal peaks in time (lagged) or in space (not reaching as far north/south). Many models are too intense (both in boreal and austral summer) plus there are shifts in peaks, but not necessarily in equatorial tropics.

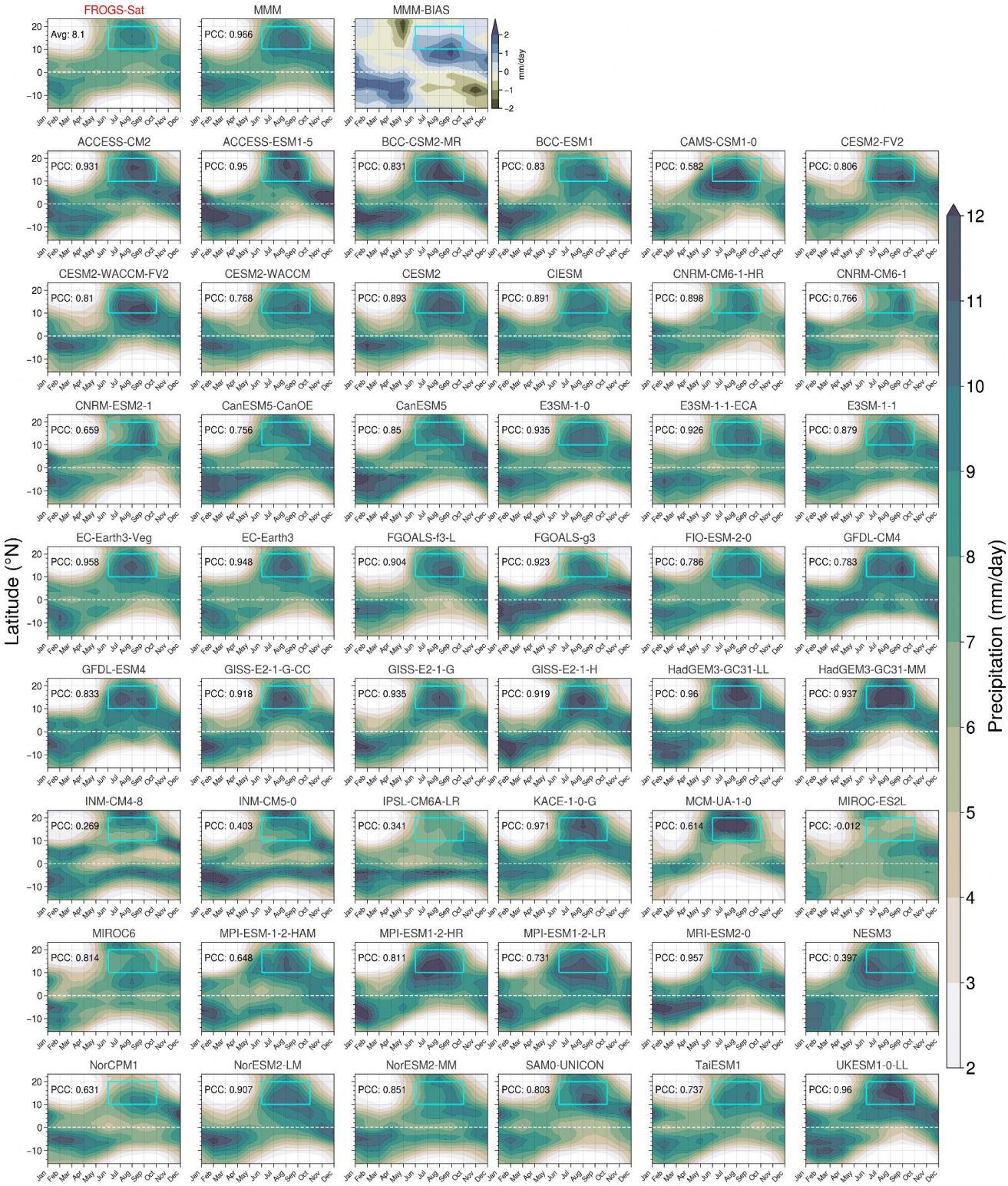

Figure 5.14: The time-latitudinal progression of zonally-averaged (80-160E) climatological monthly precipitation (i.e. passage of the ITCZ-monsoon rain belt) for the period 1995-2014. (Top row) Multi-satellite-mean observations from the FROGS database (FROGS-Sat), the multi-model mean (MMM) and the bias in the MMM (MMM-Bias). The 48 CMIP6 models are individually shown in subsequent rows. Also shown is the pattern correlation coefficient (PCC) value between each model and FROGS computed over the cyan box (June-October, 10-20N, representing the boreal summer monsoon season). The area average represented by the cyan box is shown for FROGs (8.1 mm/day).

Figure 5.15 shows the ranked pattern correlation values comparing zonally-averaged climatological monthly rainfall from each CMIP6 GCM with satellite observations for the June to October period across 10-20N. It can be seen from the figure that many of the CMIP6 GCMs perform quite well in simulating monsoons with around 18 of them having PCC of more than 0.9. Based on the monsoon PCC shown here the bottom 5 models are MIROC-ES2L, INM-CM4-8, IPSL-CM6A-LR, NESM3, and INM-CM5-0.

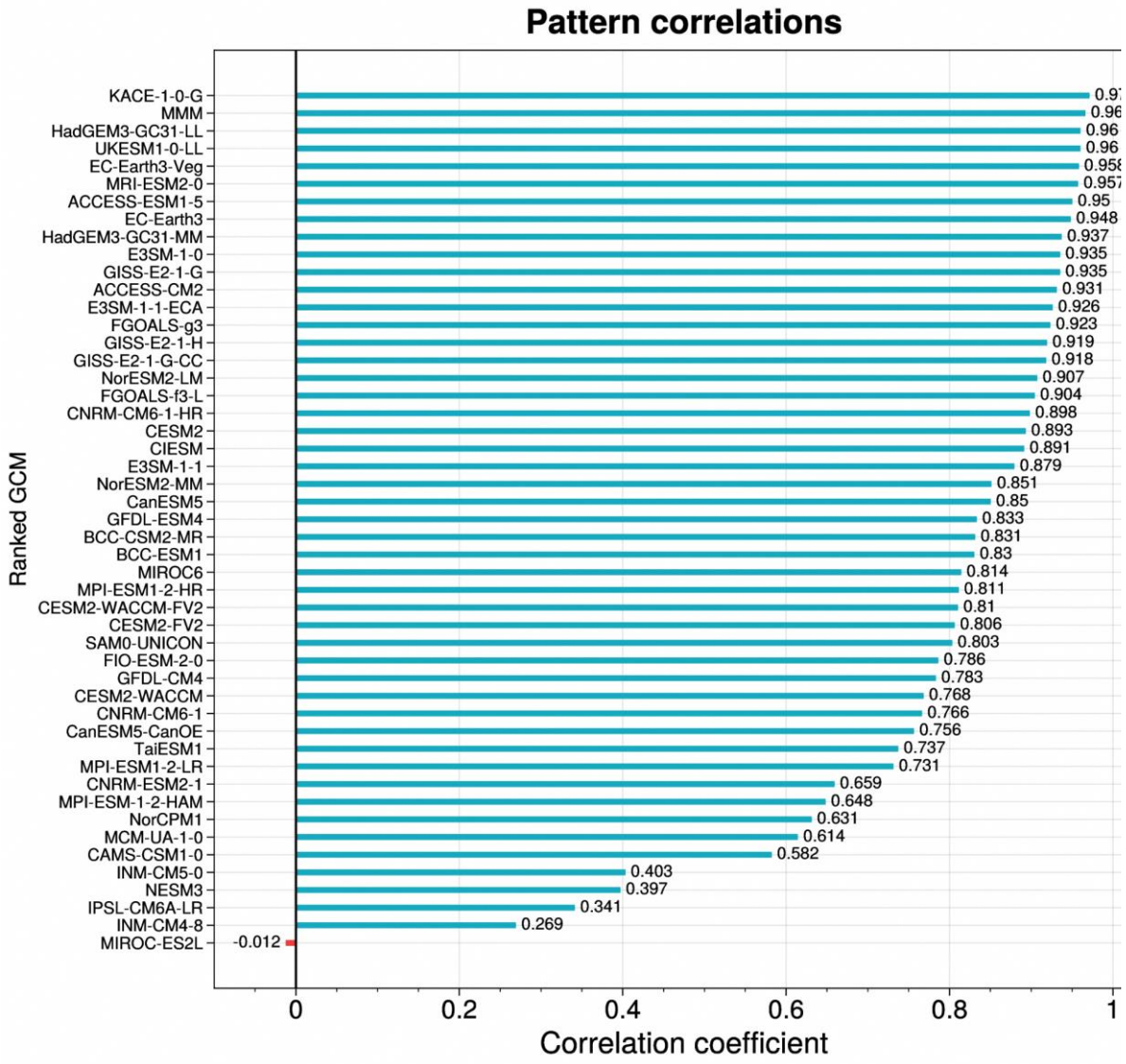

Figure 5.15: Ranked pattern correlation values comparing zonally-averaged climatological monthly rainfall from each model with satellite observations for the boreal summer monsoon period (June to October) across 10-20N.

In Figure 5.16 we show the normalised model bias in area average rainfall during the Jun-Oct period relative to satellite observations. We can see from the figure that 38/48 models show wet bias, with a considerable spread that varies in the range 2-36%. Overall, the multi-model mean (MMM) shows 9% wet bias, and shows really good pattern correlation (0.966; Figure 5.15). This is consistent with other studies (e.g., Martin et al. 2021) that show models tend to underestimate rainfall over the Indonesian island region in JJA and overestimate it over the region of the South China Sea and western Pacific (this is particularly prevalent in the HadGEM3 family of models).

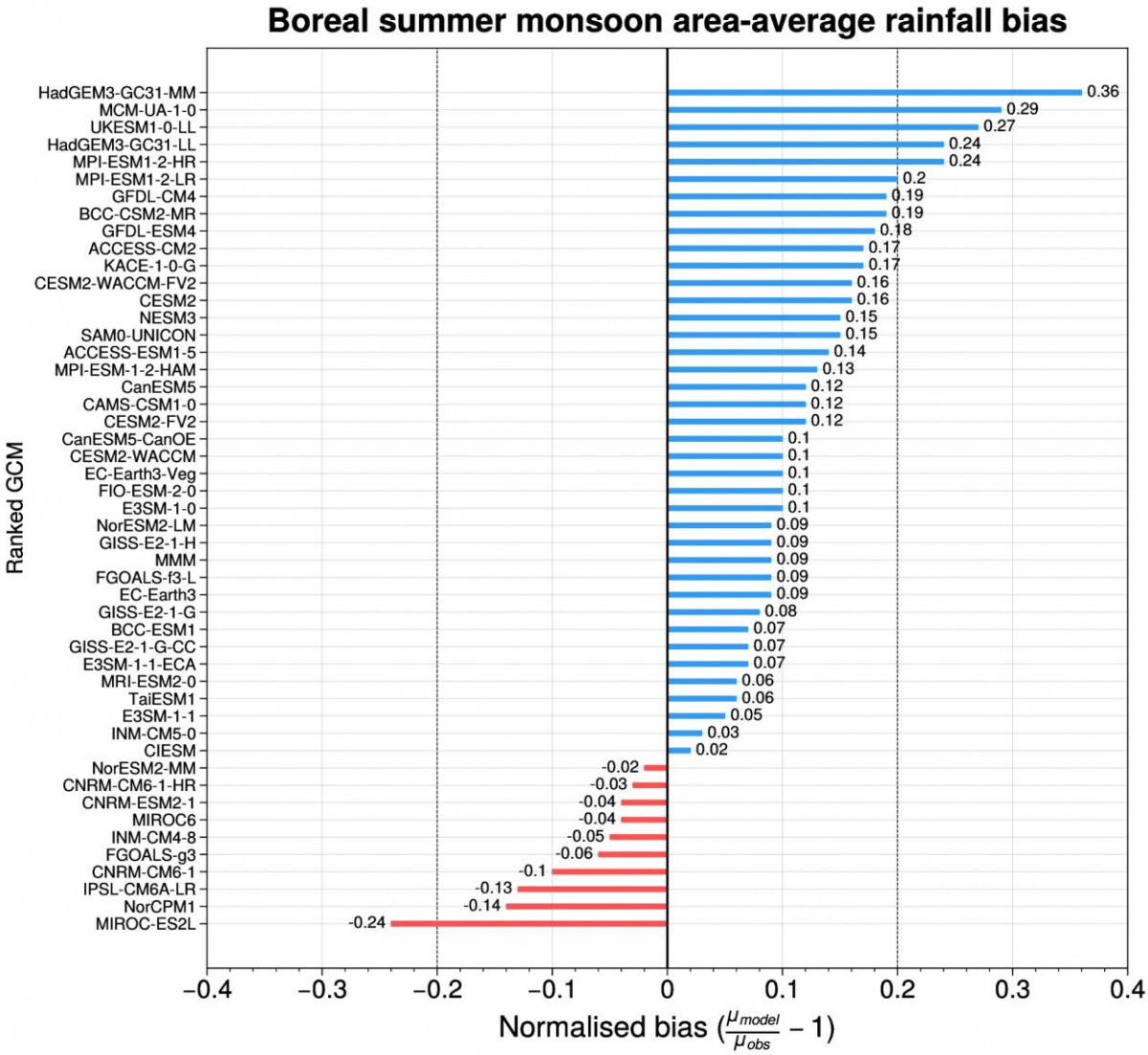

Figure 5.16: Normalised model bias in areal average rainfall during the boreal summer monsoon period (Jun-Oct) relative to satellite observations across 10-20N.

Unlike the off-equatorial tropics, the ITCZ crosses the equatorial zone both during the northward and southward movement, hence providing a somewhat different flavour to the monsoons. In Figure 5.17 we show the climatological (1995-2014) annual cycle of rainfall area-averaged over the equatorial region 80–160E, -2.25–2.25N from observations and from CMIP6. For the CMIP6 GCMs we show the multimodel mean (MMM), multimodel maximum (MMX) and multimodel minimum (MMN). Although there is a large diversity in the models as can be seen from the difference between the MMX and MMN, overall, the MMM resembles the both satellite rainfall (FROGS) over the region and the station-based rainfall annual cycle quite well. This is further confirmed from the DJF spatial pattern of rainfall from FROGS and MMM.

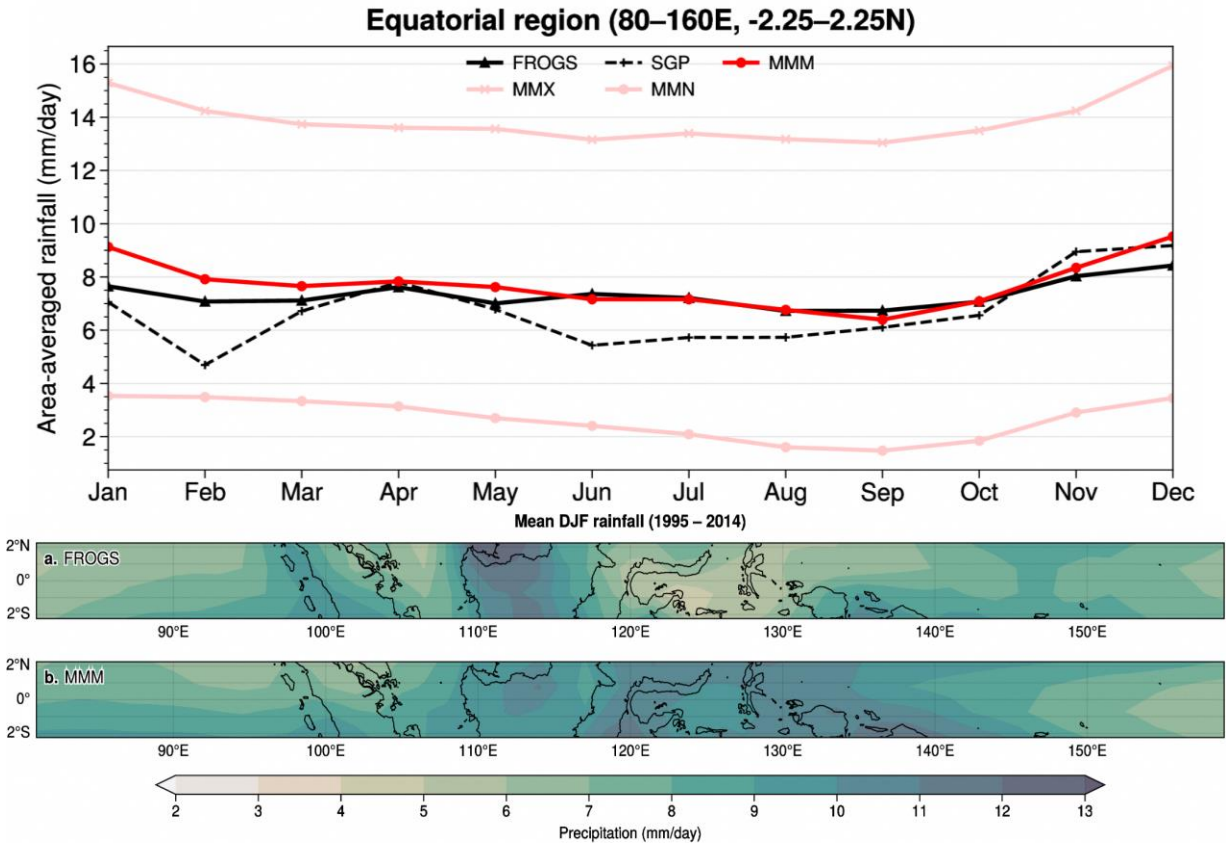

Figure 5.17: (Top panel) Climatological (1995-2014) annual cycle of rainfall area-averaged over the equatorial region 80–160E, -2.25–2.25N in the FROGS multi-satellite and CMIP6 multimodel mean (MMM), multimodel maximum (MMX) and multimodel minimum (MMN). The climatological annual cycle over Singapore (28-station average) is shown for comparison. The bottom panel shows the DJF rainfall from FROGS and MMM.

Monsoons are traditionally associated with a reversal of low-level winds, turning from easterlies to monsoon westerlies upon the arrival of the first strong monsoon surge. Figure 5.18 shows this for regions north and south of the equator indicating the climatological monsoon onset to be in May for the northern hemisphere and December for the southern hemisphere monsoon periods. Looking at the equator, the passing over of the ITCZ twice a year creates a different situation with winds being (a) generally weak throughout the year and (b) only weak wind reversals with mostly climatological weak westerlies for most months. The multi-model mean from the CMIP6 GCMs performs quite well in simulating the overall annual cycle and the May and December monsoon onsets in the northern and southern hemispheres, respectively.

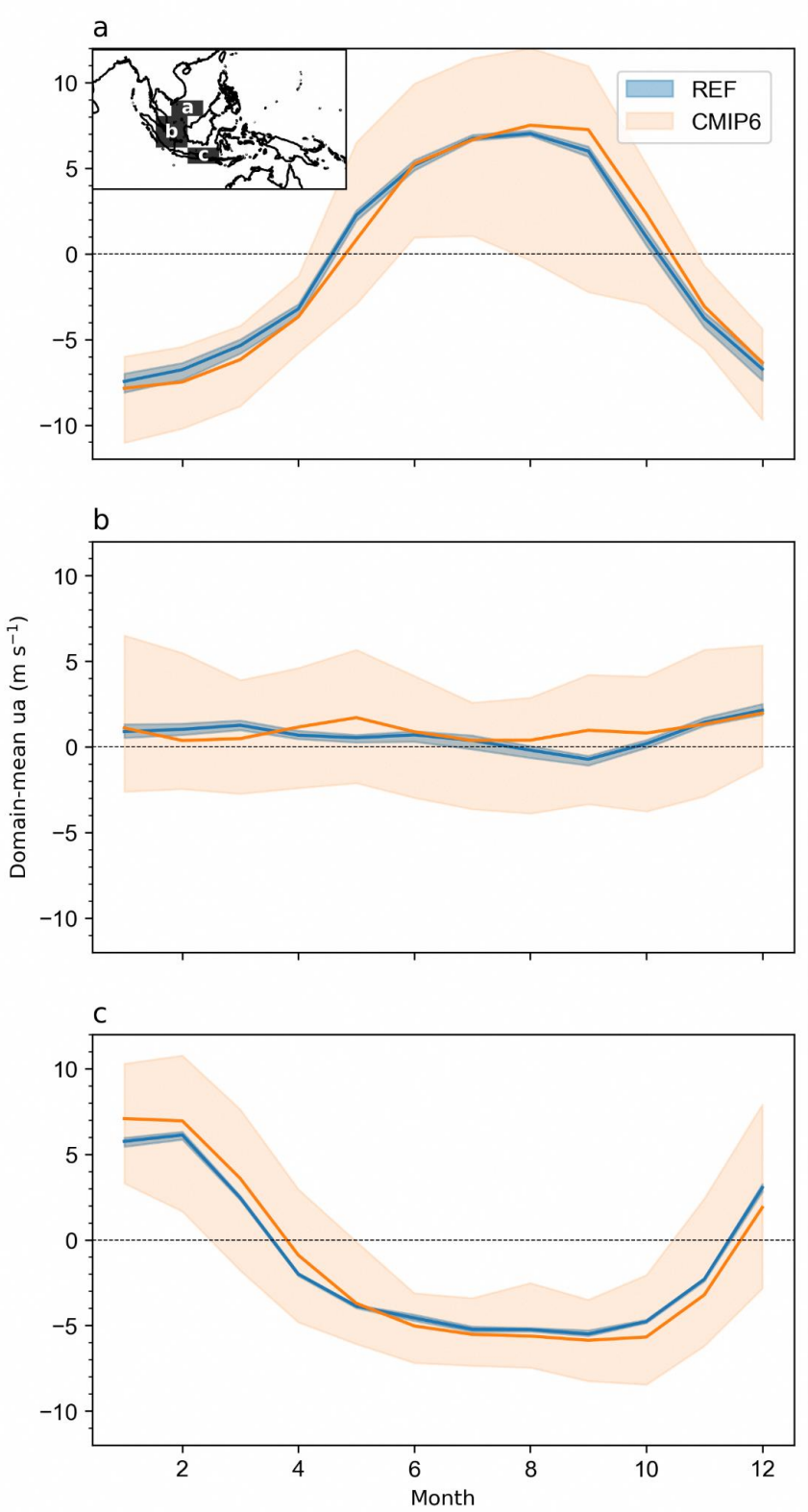

Figure 5.18: Domain mean of climatological (1995-2014) zonal wind at 850 hPa over (a) 110E to 115E, 5N to 10N (b) 100E to 110E, 5S to 5N, (c) 110E to 120E, 10S to 5S. The three domains are shown in the inset in (a). The shading shows the full range of the reference reanalysis datasets (ERA5, JRA55, MERRA2) as well as 49 CMIP6 models.

5.4.2 ENSO

ENSO is associated with the equatorial Pacific Ocean variability influencing atmospheric processes remotely and thereby one of the most important climate drivers that influences year to year variability of temperature and rainfall across the Maritime Continent (Juneng and Tangang 2005). Across the Indo-Pacific Ocean, ENSO induces a zonal dipole pattern of precipitation variability, i.e., positive variability in the Tropical Pacific (TP) and "horseshoe" shaped negative variability towards the MC (Langenbrunner and Neelin 2013). That is, TP becomes wetter than normal while MC becomes drier. Physically, ENSO-rainfall teleconnection over the MC is part of the ENSO-induced circulation responses over the tropics (Wang et al. 2003; Lau and Nath 2003; Stuecker et al. 2015).

In boreal summer when El Niño develops, a sequence of evolution begins with the eastward shifting of Walker Circulation due to the anomalous warming in eastern Pacific. The shift suppresses convection over the MC (also weakens Asian–Australian Monsoon) and enhances convection in the Central Pacific. Also note that the ENSO evolution during summer depends on what has happened in the previous boreal winter.

Here we investigate GCM's performance on ENSO, and we mainly focus on the climatology of ENSO amplitude, frequency, and its teleconnection. ENSO also varies from decade to decade, not only in amplitude and frequency (Wittenberg 2009) but also in its diversity and asymmetry characteristics (Chen et al. 2017). To provide a more reliable evaluation for ENSO interannual variability, we choose a longer 30-year period (1985-2014) as the study period instead of using 1995-2014 (20-year chosen by IPCC AR6).

ENSO Amplitude

Here as part of the evaluation for regional downscaling, we briefly investigate whether CMIP6 models can simulate reasonable realistic amplitude for ENSO. ENSO amplitude is normally represented using the DJF season standard deviation of the Nino3.4 index. This amplitude varies largely across different ENSO events (e.g., weak, moderate, and extreme events) as part of the natural variability of the ocean state. Additionally, simulations of these events show variations across these climate models (e.g, Chen et al. 2017) which originate from model-internal sources. Future projection for ENSO amplitude is also very uncertain (e.g., Beobide-Arsuaga et al. 2021) because of the difficulties in estimating how the natural variability might change as well as the remote teleconnections associated with ENSO.

As can be seen from Figure 5.19, ENSO amplitude average from observation and reanalysis is 1.13°C. Model mean ENSO amplitude is 1.19°C, which is very close to the observation. We do notice a large spread across individual models, from very low (around 0.5°C) or very high (over 2°C) ENSO amplitude. Based on ENSO amplitude the bottom 6 models are INM-CM4-8, CNRM-CM6-1-HR, INM-CM5-0, CESM2-FV2, MIROC-ES2L, and NorESM2-MM.

ENSO Frequency

ENSO generally occurs every 2 to 7 years (Cane and Zebiak, 1985). Studies suggested that extreme El Niño and La Niña events in CMIP5 models will occur more frequently in a changing climate (Cai et al. 2014, 2015). However, as to frequency of all ENSO events, many studies concluded that ENSO frequency changes are strongly model-dependent, and the model consensus is not robust on how ENSO frequency will change in a changing climate (Guilyardi (2006), Callahan et al. (2021)).

Given that ENSO tends to peak during boreal winter (DJF season), here we use the index Y=DJF season averaged Niño3.4 anomaly, and we define a threshold TH=0.6 X standard deviation of Y. Thus a given year is considered to be in an El Niño state when Y>TH. The year in a La Niña state is when Y<-TH. The year in the neutral state is when -TH<=Y<=TH. Note that we classify individual years instead of months. Also note that we do not use a fixed threshold rather a model-dependent threshold. For HadISST, the threshold is 0.68°C, ERA5's threshold is 0.74°C, and MERRA2's threshold is 0.68°C.

We define the frequency of El Niño years (FEN) as the number of El Niño years divided by the total number of years. We also define the frequency of La Niña years (FLN) and the frequency of neutral

years (FNEU) in a similar way, and FEN+FLN+FNEU=1. It is known that El Niño occurs every 2 to 7 years, such that 0.14<FEN<0.5. As can be seen from Figure 5.20, from observations and reanalysis, for El Niño, observation mean frequency is 0.3. For models, multi-model mean for El Niño FEN_model=0.29, which is very close to the observation and reanalysis. Models have a spread as to the frequency, from 0.15 to 0.4. Based on the ENSO frequency the bottom few models are KACE-1-0-G, CanESM5, IPSL-CM6A-LR, CESM2-WACCM-FV2, FGOALS-g3, and GISS-E2-1-G-CC.

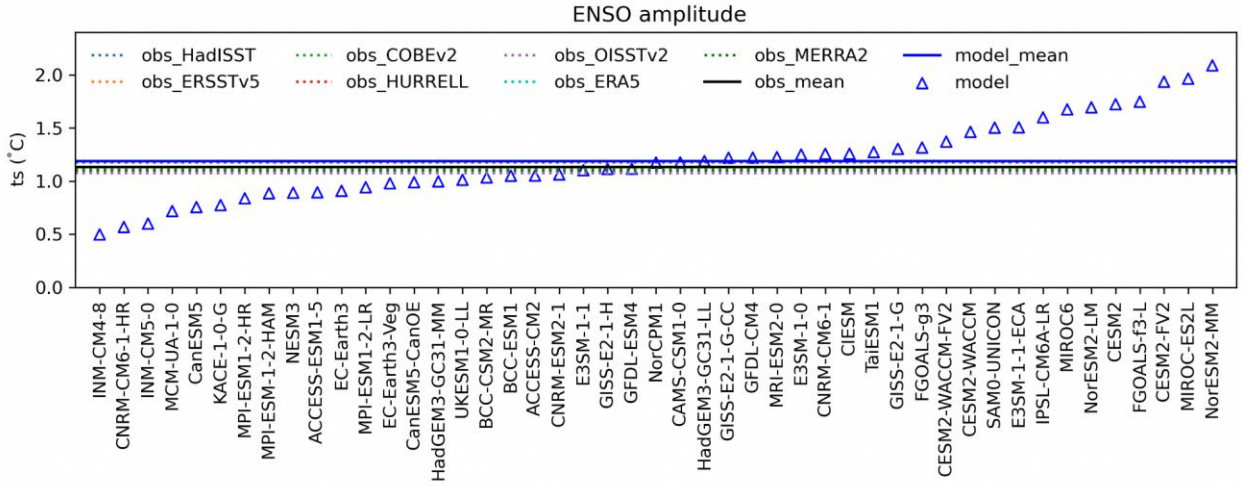

Figure 5.19: ENSO amplitude defined as standard deviation of Nino3.4 index (1985-2014 DJF mean).

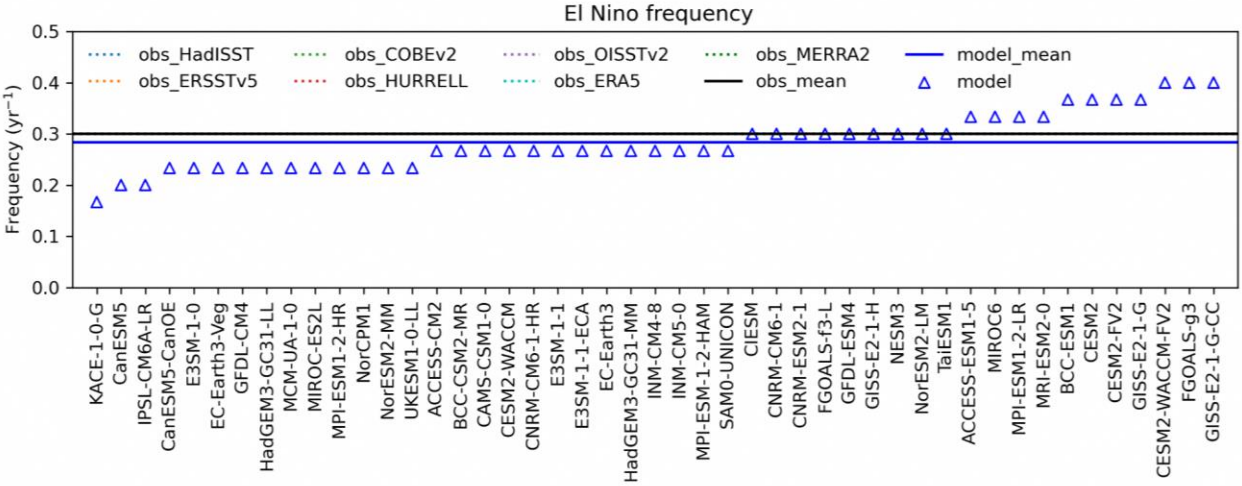

Figure 5.20: The frequency of El Niño for 47 CMIP6 GCMs and from observations and reanalysis from 1985 to 2014. Also shown are the ensemble mean for models and for observations and reanalysis.

ENSO Teleconnection

ENSO has impacts on worldwide precipitation variabilities (Ropelewski and Halpert 1987). Across the Indo-Pacific Ocean, a zonal dipole pattern of precipitation variability occurs during El Niño, i.e., positive variability in the Tropical Pacific (TP) and “horseshoe” shaped negative variability towards the Maritime Continent (MC) (Langenbrunner and Neelin 2013). That is, TP

becomes wetter than normal while MC becomes drier. In boreal summer when El Niño develops, a sequence of evolution begins with the eastward shifting of Walker Circulation due to the anomalous warming in eastern Pacific. The shift suppresses convection over the MC (also weakens Asian–Australian Monsoon) and enhances convection in the Central Pacific (Wang et al. 2003; Lau and Nath 2003; Stuecker et al. 2015).

As to the model performance on the ENSO teleconnection over the MC and Western Pacific, both CMIP5 and CMIP6 models tend to underestimate the negative rainfall teleconnection over the Central Maritime Continent but overestimate the positive ENSO rainfall teleconnection in the western Pacific and Eastern Maritime Continent (Jiang et al. 2022). Here, as part of the model evaluation for regional downscaling, we evaluate the performance of ENSO-rainfall teleconnection over the Tropical Pacific and the Maritime Continent in CMIP6 models and show it in Figure 5.21. We define the domain averaged rainfall and calculate the lag-0 correlation and covariance between the rainfall and the Niño3.4 TS anomaly (divided by one standard deviation of SST to only retain the pr unit of mm/day). We use the HadISST ts and GPCP rainfall as the observation benchmark.

We find that models perform well for the TP region. However, models overestimate the rainfall variability over the eastern MC but underestimate the El Niño-induced rainfall variability over the central MC. It is due to the westward extension of the cold tongue bias that pushes the surface temperature and rainfall variability from the western Pacific to the MC. For the CMC during the JJA season, observed rainfall variability is -0.51 mm/day, and model variability is -0.26 mm/day (0.25 mm/day weaker than the observation). During the DJF season, observed rainfall variability is -0.81 mm/day, and model variability is -0.46 mm/day (0.35 mm/day weaker than the observation).

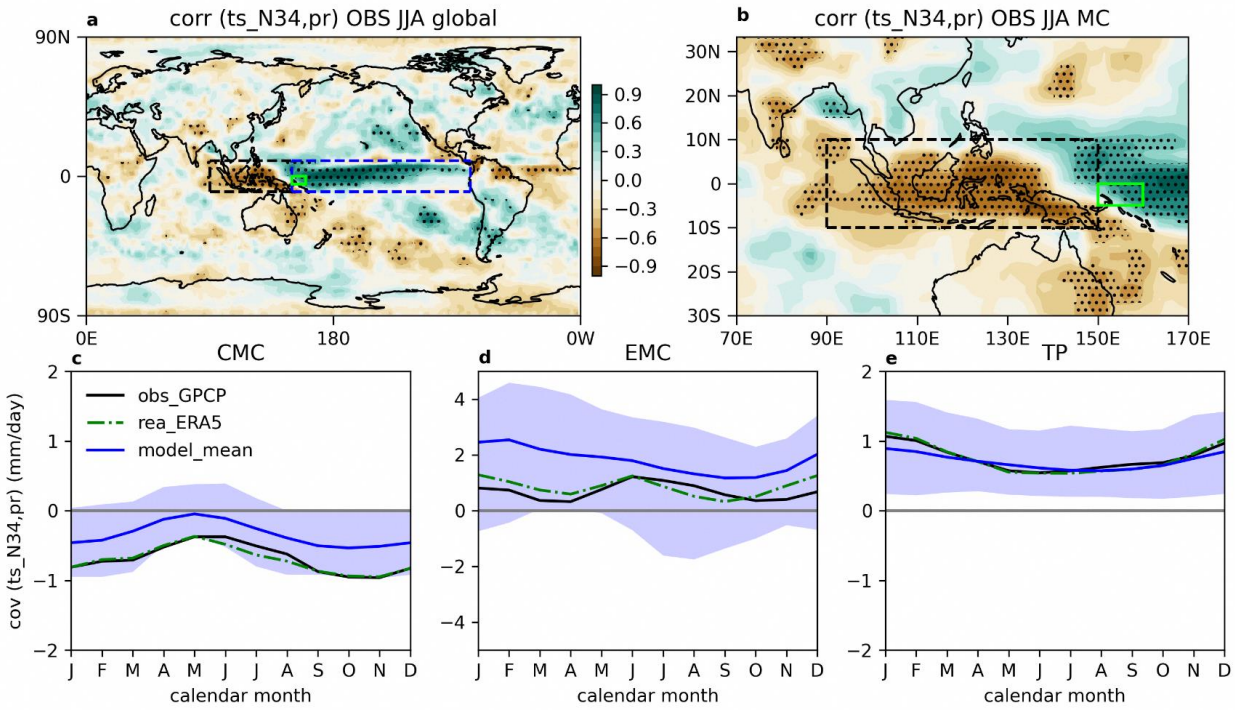

Figure 5.21: ENSO-rainfall teleconnection in the observation and CMIP6 models. a. Observed global ENSO-precipitation correlation coefficient during boreal summer (JJA). Here the correlation coefficient is calculated between the anomalous precipitation (pr) and Niño3.4 sea surface temperature (TS). Stippled area indicates significant correlation with p-value<0.01. Defined domains of Central Maritime Continent (CMC) (black dashed box), Eastern Maritime Continent (EMC) (green box), and tropical Pacific (TP)(blue dashed box) are shown. b. similar to a, but focusing on the MC. c-e shows the model performance as to the ENSO-rainfall teleconnection. c. 12-month covariance between the Niño3.4 TS and the CMC domain-averaged

precipitation. Observations (GPCP, black curve), reanalysis (ERA5, green dashed curve), and the multi-model mean of 32 CMIP6 models for the historical period (blue curve) are shown. The shade covers the 95% model range. d. similar to c but showing the EMC domain. e. similar to c but showing the TP domain.

5.4.3 IOD

The Maritime Continent is in between the Indian Ocean and Pacific Ocean and is affected by the ocean state in both. Hence, we also evaluate model performance over the Indian Ocean. We define the IODe index =ts averaged over the eastern IO [90E-110E, 10S-0S]. IODw index= ts averaged over the western IO [50E-70E, 10S-10N]. Then we define the IODemw index=IODe minus IODw, which indicates the zonal ts gradient.

We analyzed the amplitude of IOD, defined as one standard deviation of the monthly ts anomaly in IODemw. Observed IOD amplitude is 0.4°C, model mean IOD amplitude is 0.52°C (0.12°C stronger). Here models tend to have slightly stronger variability than the observation (Figure 5.22). Based on IOD amplitude the bottom few models are the 2 INM models, TAIESM-1, SAM0-UNICON, and CESM-FV2.

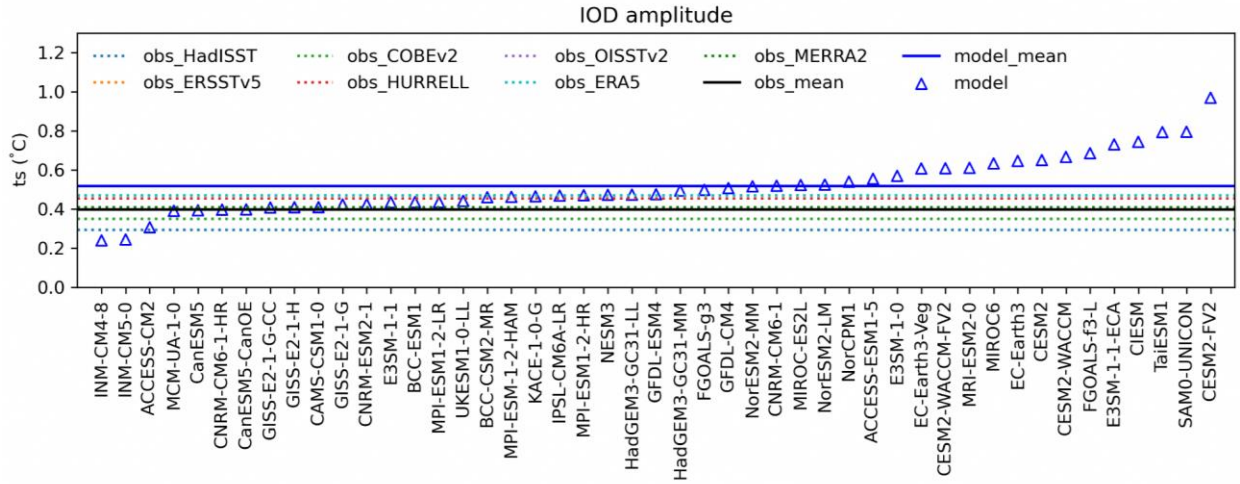

Figure 5.22: IOD amplitude in observations (mean in black line) and models (mean in black line). IOD amplitude is calculated using one standard deviation of the IODemw index (annual mean, 1985-2014).

5.4.4 Equatorial Pacific Cold Tongue

Here we define an index to measure the overall equatorial Pacific ts. TPI =whole equatorial Pacific averaged over [150E-280E 5N-5S]. Within the TP, the warm pool is on the western side, and the cold tongue is on the eastern side. Here we define the CTI index = averaged ts over the cold tongue region [180°E-270°E,5°N-5°S]. The zonal ts gradient is also an important dynamical feature to simulate. Here we define a CTGI=cold tongue gradient index =CTI-TPI, annual mean from 1985 to 2014. CTGI tells the cold tongue ts relative to the whole equatorial Pacific. annual mean observation CTGI is -0.54°C. Model mean CTGI is -0.62°C (-0.08°C slightly stronger cold tongue relative to the whole TP, also indicating a stronger zonal ts difference) (Figure 5.23). This stronger cold tongue in models is associated with a stronger zonal wind and westward extension of the cold tongue into the warm pool. Based on the equatorial Pacific cold tongue bias, the bottom few models are MPI-ESM1-2-HR, NorESM2-LM, GISS-E2-1-G, and GISS-E2-1-G-CC.

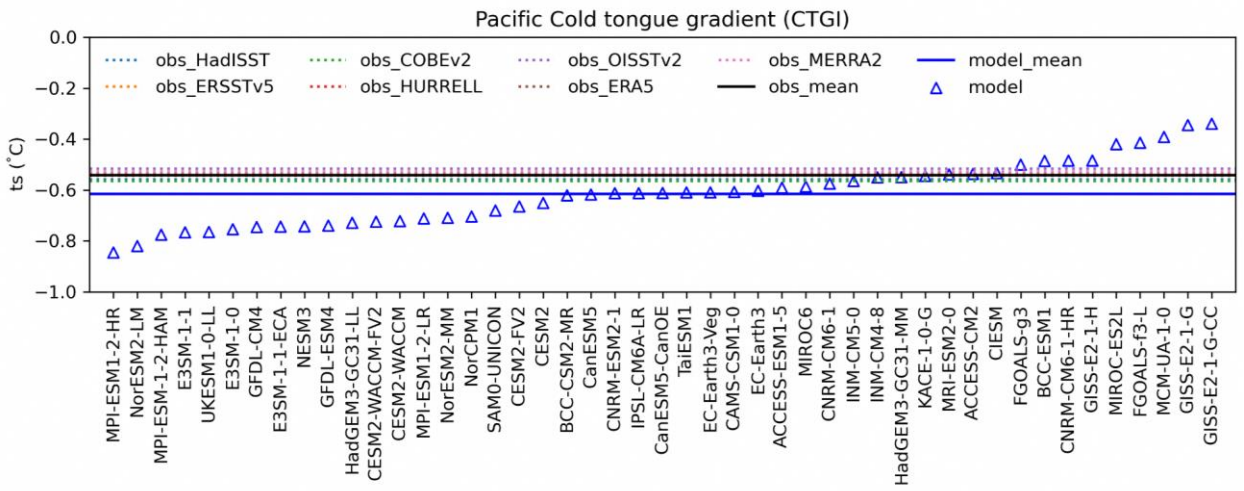

Figure 5.23: Pacific cold tongue gradient index (CTGI) in observation and models (1985-2014). The negative value indicates the eastern cold tongue area is cooler than the western warm pool.

5.4.5 Northeast Monsoon Surge

Northeast monsoon surges are a key synoptic feature of the boreal winter circulation over the Maritime Continent (e.g. Chang et al., 2005) and can lead to extreme rainfall. These surges can also be enhanced by the presence of a favourable phase of the MJO (e.g. Lim et al., 2017) and might also aid the MJO in its passage across the Maritime Continent (Pang et al., 2018). Given the importance of boreal winter monsoon cold surges to the weather and climate of SEA, the performance of CMIP6 models in simulating cold surges is quite relevant to the evaluation and subsequent sub-selection for dynamical downscaling.

Most of the existing literature on boreal winter cold surges over the Maritime Continent have focused on their observed characteristics, with relatively little mentioned on their simulation in models. An earlier analysis of CMIP5 models (McSweeney et al., Appendix 3 of V2) reported that the easterly component of surge winds were too strong in some models relative to the northerly component, with the flow directed towards Vietnam rather than southwards, while a more recent study by Xavier et al (2020) found that the UKMO Global Atmosphere 7.0 (GA7.0) and Global Coupled 3.0 (GC3.0) configurations of the Unified Model yield a dry bias in the simulation of surge rainfall.

In Figure 5.24 we present the evaluation of cold surge simulations in CMIP6 models, defined in Chapter 3.7. Based on reanalysis data, one can see from Figure 5.24a that the north-easterly winds over the South China Sea turn north-westerly after crossing the equator, together with high rainfall, especially over Philippines and Borneo. Figure 5.24b shows that the models are able to capture the general flow of the surge winds, including the turning at the equator. The easterly bias flagged in (McSweeney et al., Appendix 3 of V2) is not immediately obvious in the individual models (figure not shown), with the caveat that their analysis was performed using a fixed wind speed threshold, whereas this analysis uses a threshold that is tied to the mean and standard deviation of each model.

Models generally have a wet bias over Sulawesi and a dry bias over the Philippines (Figure 5.24c), possibly related to the model resolution of the topography of the Philippines. Models generally underestimate the rainfall over the Indian Ocean, with the multi-model anomalous winds directed over the Indian subcontinent. Over the Western Maritime Continent, rainfall bias can be either positive or negative. Models generally underestimate the percentage of surge days in NDJF (19% in REF), with 32 out of 36 models used for this analysis, exhibiting frequencies from 15 to 19%, and four models below 15%: AWI-ESM-1-1-LR (14%), FGOALS-f3-L (14%), KACE-1-0-G (12%) and TaiESM1 (8%).

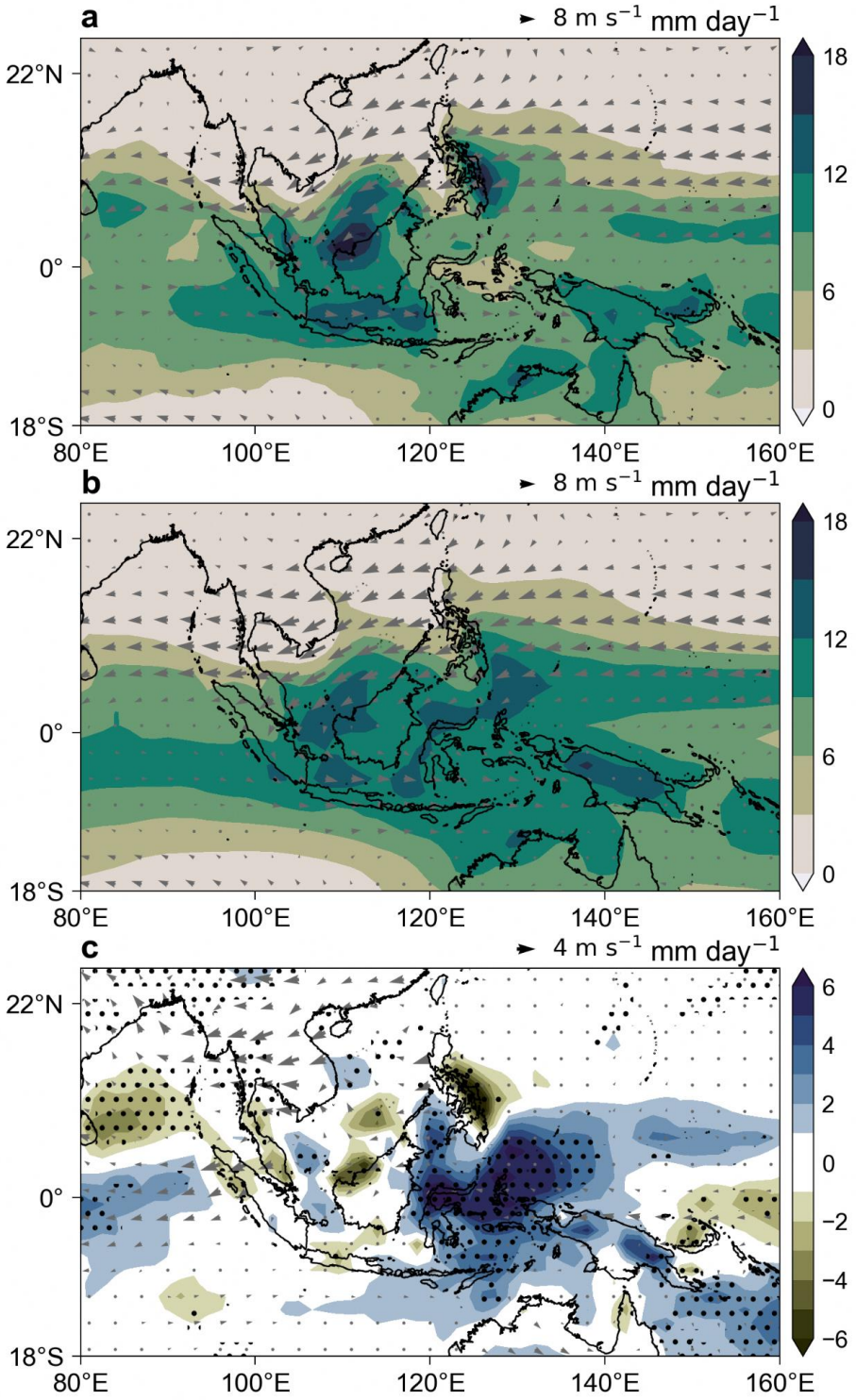

Figure 5.24: (a) Precipitation and 850 hPa winds composited over surge days in REF (winds and PSL are derived from the ensemble mean of ERA5, MERRA2, and JRA55, precipitation the ensemble mean of 5 datasets from FROGs: CMORPH, GSMAP, IMERG, PERSIANN-CDR, and TRMM 3B42). (b) As in (a), but for 36 CMIP6 models. (c) Model bias in surge precipitation and winds (i.e. (b) - (a)).

5.4.6 MJO

The Madden-Julian Oscillation (MJO; Madden & Julian, 1971, 1972), characterized by an eastward-propagating large-scale band of convection from the Indian Ocean to the central Pacific, is one of the important climate drivers affecting global weather and climate, and especially the Maritime continent region (e.g., Lim et al. 2017). However, representing the MJO in climate models has been a challenge. In a recent study, Chen et al. (2021) evaluated the simulation of MJO in CMIP5 and CMIP6 models and reported that the MJO characteristics are better reproduced in CMIP6 with a corresponding decrease in inter-model spread in biases. However, there still are existing biases in CMIP6 models, such as, underestimation of frequency of initiation, underestimation of amplitude, and overestimation of the MC barrier effect on MJO propagation speeds. From CMIP5 to CMIP6, while some models have improved skills, some others have degraded. Le et al., (2021) reported that the MJO-related precipitation over the MC is still underestimated in CMIP6 models.

While various metrics have been used in the literature to evaluate the performance skill in models, one of the widely used metrics used for evaluation is the Eastward/Westward power ratio (E/W ratio hereafter). This metric indicates the robustness of eastward propagating feature of the MJO (Zhang and Hendon 1997), and has been widely used in observational (e.g., Zhang and Hendon 1997; Hendon et al. 1999) and modelling studies (e.g., Lin et al. 2006; Kim et al. 2009). In Figure 22 we show the E/W ratio for the months November-April over the period 1995-2014 using precipitation from GPCP v1.3 as the baseline and compare the same with CMIP6 models.

While the observed ratio is around 2.8, in models it can vary from less than 1 (westward propagating) to more than 5 (strongly eastward propagating). From this figure, some CMIP6 models, namely, CanESM5, INM-CM4-8, and INM-CM5-0 can clearly be discarded as they show a westward propagating MJO. Most of the models show an E/W ratio lower than observed, and hence a slower eastward propagation, maybe due to stronger barrier effect of the MC.

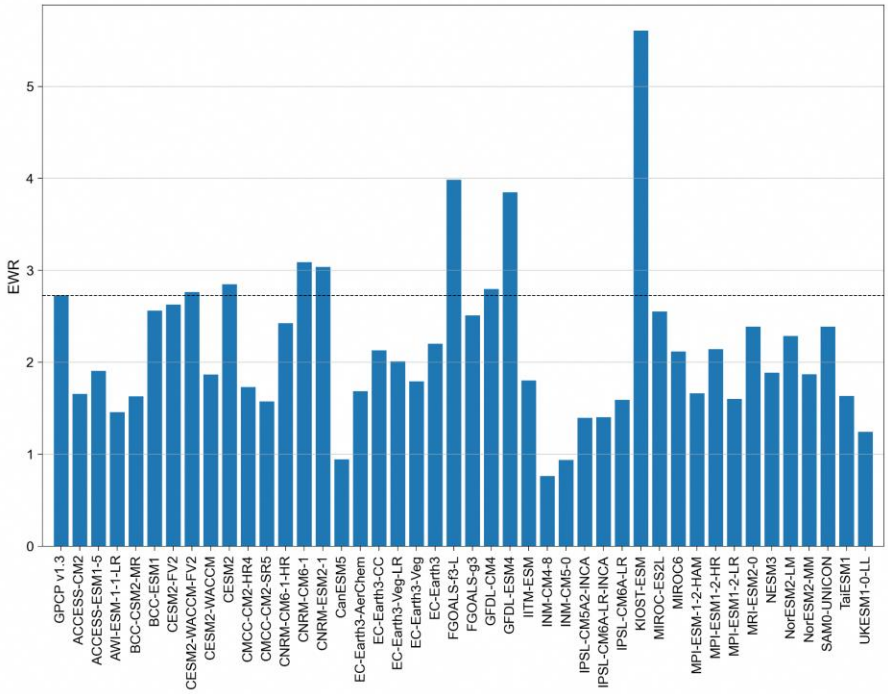

Figure 5.25: East-West power ratio of CMIP6 GCMs for November-April from 1995 to 2014 compared to GPCP v1.3.

5.5 Model Independence

Following Brunner et al (2020), Table 5.3 shows the CMIP model families built on similar internal schemes for atmosphere, ocean, etc. It has been shown in some past studies that the CMIP model archive is not an archive of completely independent models. This raises the question about independent realisations of future climates and in general the understanding is that the CMIP ensemble is a somewhat 'degenerated' ensemble of future states.

Table 5.3: CMIP6 model families based on the genealogy reported in Brunner et al. (2020) using 33 models. The genealogy is computed based on the global mean surface-air temperature and mean sea level pressure. Models in bold were selected for downscaling.

Model Family	Models belonging to specific family	Common family feature
1	CanESM5-CanOE, CanESM5	Built within ONE modelling centre on similar schemes
2	CESM2-WACCM, CESM2, **NorESM2-MM**, FIO-ESM-2-0	Built on NCAR's atmosphere model
3	CNRM-ESM2-1, CNRM-CM6-1, CNRM-CM6-1-HR	Built within ONE modelling centre on similar schemes
4	EC-Earth3-Veg, **EC-Earth3**	Built within ONE modelling centre on similar schemes
5	FGOALS-f3-L, FGOALS-g3	Built within ONE modelling centre on similar schemes
6	INM-CM5-0, INM-CM4-8	Built within ONE modelling centre on similar schemes
7	MIROC-ES2L, **MIROC6**	Built within ONE modelling centre on similar schemes
8	MPI-ESM1-2-LR, **MPI-ESM1-2-HR**, AWI-CM1-1-MR, NESM3	All using ECHAM-like atmosphere model
9	**UKESM1-0-LL**, HadGEM3-GC31-LL, **ACCESS-CM2**, KACE-1-0-G, ACCESS-ESM1-5	All using the UM as a core atmospheric model system
NA	GFDL-CM4, GFDL-ESM4, MRI-ESM2-0, CAMS-CSM1-0, GISS-E2-1-G, BCC-CSM2-MR, IPSL-CM6A-LR, MCM-UA-1-0	More distant association with some of the other families

In order to provide a downscaling ensemble from as independent as possible GCMs, we have identified a number of models which are possible choices, and together with other sub-selection metrics might help identify the most suitable set of independent models to use for downscaling.

5.6 Range of Future Projections and ECS

As discussed in Chapter 4 (subsection 4.2.1), the Equilibrium Climate Sensitivity (ECS) is defined as the global- and annual-mean near-surface air temperature rise that is expected to occur eventually, once all the excess heat trapped (top-of-atmosphere radiative imbalance) by the doubling of CO2 has been distributed evenly down into the deep ocean (i.e. when both the atmosphere and ocean have reached equilibrium with one another - a coupled equilibrium state).

Many CMIP6 models exhibit an ECS of 5°C or higher (Zelinka et al., 2020), much higher than the upper value of the CMIP5 range of 4.5°C. Based on the analysis of Sherwood et al. (2020), the Likely Range now range in ECS was constrained to lie in the range 2.5 - 4.0°C, down from what was reported in AR5. The IPCC also narrowed the Very Likely Range of ECS to be between 2.0 to 5.0°C, down from 1.0 to 6.0°C. The likely and very likely range of ECS in AR5 and AR6 are shown in Figure 5.26 for reference.

Figure 5.27 shows the ECS from the various available CMIP6 GCMs. The wide range of ECS can be seen from the figure with models like those from the INM showing values of less than 2oC,

whereas, there are models like CanESM5, CIESM, and HadGEM3-GC3-1-LL that have ECS values greater than 5.5oC. Ideally, we would like to span the range of ECS, while keeping other sub-selection dimensions under consideration, and also the AR6 constrained range.

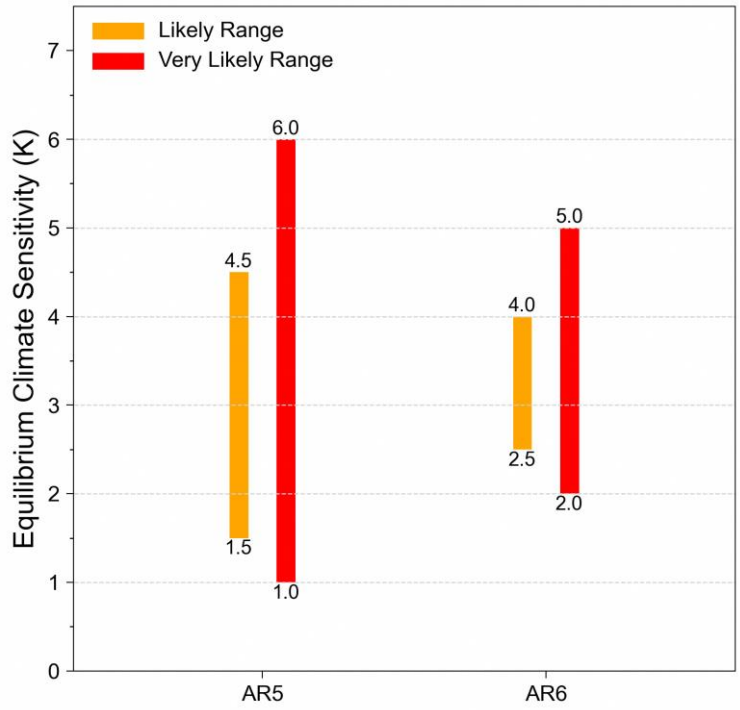

Figure 5.26: Likely and very likely range of ECS in AR5 and AR6

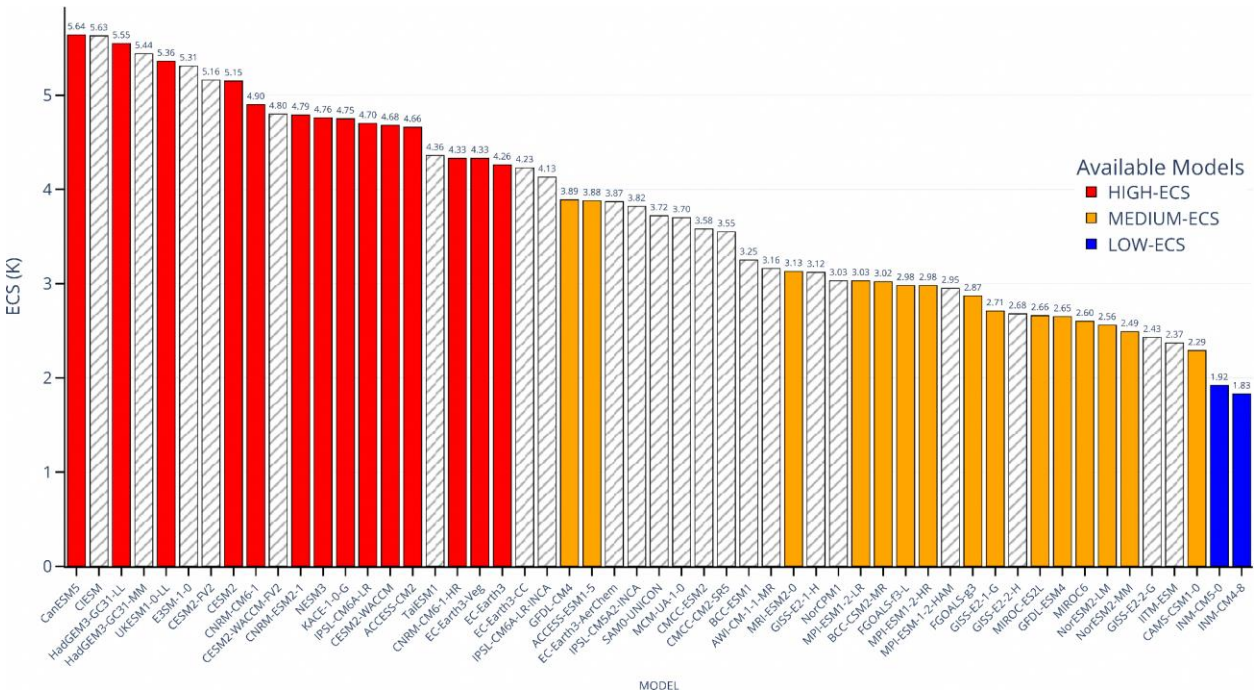

Figure 5.27: Equilibrium climate sensitivity of CMIP6 GCMs ranked high to low from left to right. The gray bars indicate models that we do not have full variable lists to analyze at the time of the V3 study.

5.7 Data Availability

For the purpose of our dynamical downscaling, we need 6-hourly profiles of temperature, zonal and meridional winds, and specific humidity (for initial conditions and lateral boundary conditions), surface pressure (for initial conditions), and 6-hourly sea surface temperatures (for initial condition and lower boundary condition). We also required that model outputs were available at 20 levels and up to at least a pressure level of 5 hPa. Where available we used the skin temperature (ts), else, a combination of surface air temperature (tas) and surface ocean temperature (tos).

An important difference in the CMIP6 archive as compared to CMIP5 is that the sub-daily data is not a part of the core delivery of the DECK experiment as well as scenario-MIP. Hence, a lot of modelling groups chose not to save and upload sub-daily data to the Earth System Grid Federation (ESGF). Since we need sub-daily data for our dynamical downscaling, this criteria plays a crucial role for our sub-selection exercise. We also would like to flag this as a possible significant constraint for CORDEX dynamical downscaling experiments.

At the time when we started the downscaling of CMIP6 GCMs in late 2020, very few GCMs had all the driving variables to run our downscaling simulations. In Table 5.1 we have highlighted the list of GCMs with availability of 6-hourly forcing fields.

As an example of how data availability drives opportunities, we did consider using data from GFDL-CM4, CNRM-CM6-1-HR and HadGEM2-MM models, but couldn't access their data on the ESGF. Upon separate conversations with the modelling groups, we were also told that not all scenarios were simulated by these models.

Based on our dynamical downscaling requirement of 6-hourly data for historical (1955-2014), and 3 SSPs (SSP1-2.6, SSP2-4.5, and SSP5-8.5) for the required variables (hus, ps, ta, tos, ua, va) and pressure level data for at least 5hPa, the latest availability as of June 2023 is shown in Table 5.1. The table shows all models running ScenarioMIP and the ones highlighted are the ones having 6-hourly data for the required variables. As can be seen from the table, only 10 models have all 4 experiments covered. GCM data needs for V3 dynamical downscaling may not be very different from that of the CORDEX community, and the availability of downscaling data from only a very few models shows that this could be a major constraint for the CORDEX community as well. It is to be noted that in CMIP5 there were many more GCMs with 6-hourly data needed for dynamical downscaling.

5.8 Future climate change spread

One additional dimension for sub-selection is to ensure that the smaller ensemble of GCMs still cover as much as possible the projected range of future climate change, especially for temperature and rainfall. Figure 5.28 shows the end-century change in rainfall and temperature over SEA from 34 CMIP6 GCMs under SSP5-8.5.

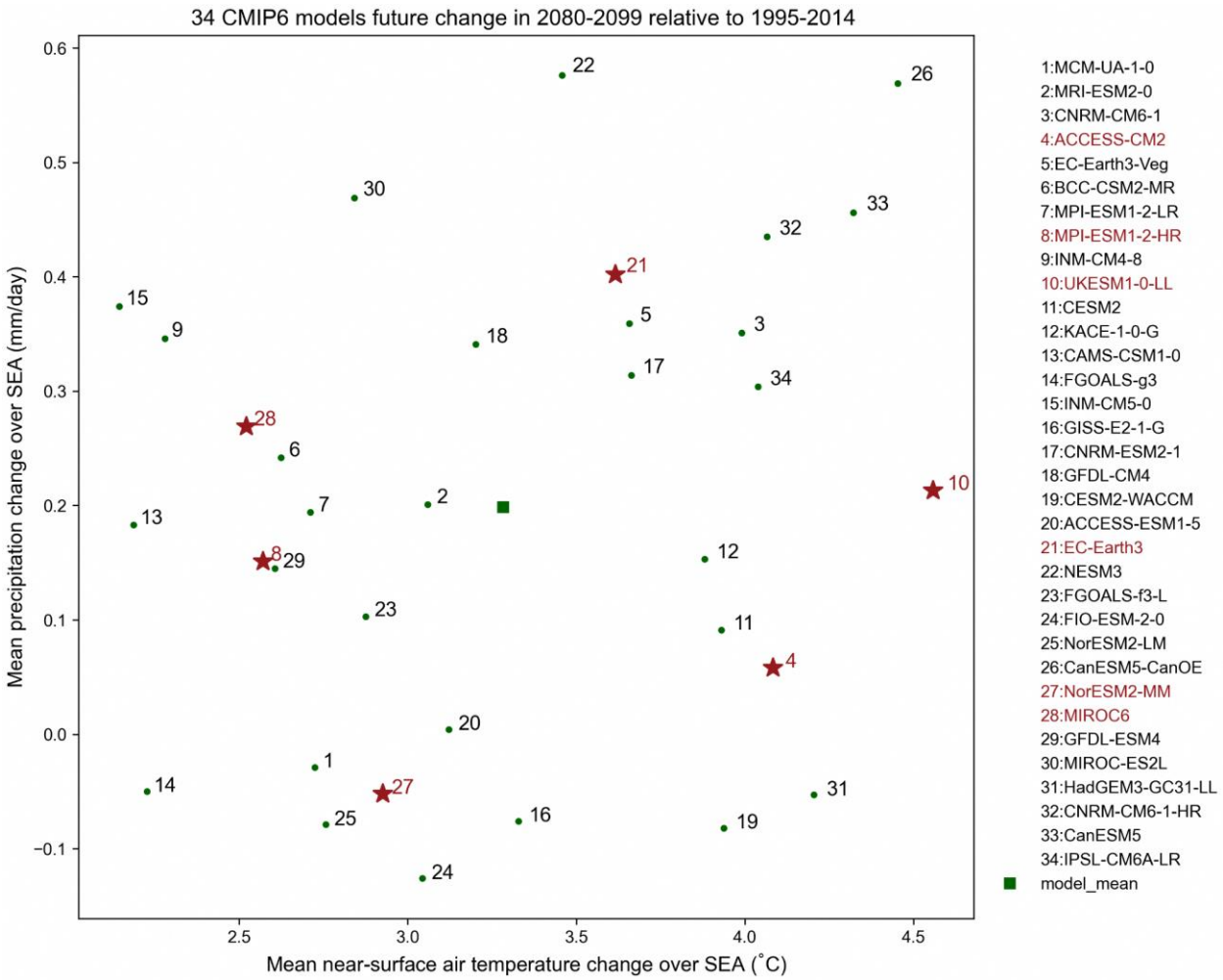

Figure 5.28: End-century (2080-2099) change (relative to 1995-2014) in rainfall and temperature over SEA from 34 CMIP6 GCMs under SSP5-8.5 (red stars denote the chosen models in our study).

5.9 Model Sub-selection

Considering all the information from the previous sections, we selected initially 8 models for further consideration based on 5.3-5.8. For our sub-selection process, we did not use any combined ranking system across all skills, rather, we mainly excluded very deficient looking models along the Tier-1 (climate variables) and Tier-2 (climate processes) skill metrics.

Combined with desired spread in ECS, independence and spread of future climates, we landed on a set of 8 models. The final list of sub-selected models are shown in Table 5.4 with the ones that made it to the final list of models that made available all the forcing data we need for downscaling highlighted in dark grey.

While we were sub-selecting the CMIP6 GCMs the various modelling groups were still in the process of uploading data to the ESGF, so we included some of the models that also had partial data and were expected to upload all of it in time. Finally, because of data availability, 3 (CNRM-CM6-1, GFDL-CM4, and HadGEM3-GC31-LL) out of the 8 models could not be used. Since we had planned to downscale at least 6 GCMs, we replaced HadGEM3-GC31-LL with a similar performing model (UKESM1-0-LL) from the same family.

Table 5.4: List of sub-selected CMIP6 GCMs for V3 Dynamical Downscaling

Sub-selected Model	ECS	Family	End-century change over SEA under SSP5-8.5 scenario	
			Precipitation (mm/day)	Temperature (°C)
ACCESS-CM2	4.66	9	0.06	4.08
CNRM-CM6-1	4.90	3	0.35	3.99
EC-EARTH3	4.26	4	0.40	3.62
GFDL-CM4	3.89	Independent	0.34	3.20
HadGEM3-GC31-LL	5.44	9	-0.05	4.21
MIROC6	2.60	7	0.27	2.52
MPI-ESM1-2-HR	2.98	8	0.15	2.57
NorESM2-MM	2.49	2	-0.05	2.93

While we were sub-selecting the CMIP6 GCMs the various modelling groups were still in the process of uploading data to the ESGF, so we included some of the models that also had partial data and were expected to upload all of it in time. Finally, because of data availability, 3 (CNRM-CM6-1, GFDL-CM4, and HadGEM3-GC31-LL) out of the 8 models could not be used. Since we had planned to downscale at least 6 GCMs, we replaced HadGEM3-GC31-LL with a similar performing model (UKESM1-0-LL) from the same family.

5.10 Summary and Discussion

For the purpose of regional climate change projections it is desirable to cover as much as possible various sources of uncertainty in order to design adaptation options that cover a wider range of climate change risks. In regard to regional climate change projections, a large amount of uncertainty often comes from the choice of scenario. It is advisable to either choose a low/high (as was done in V2) or a low/medium/high set of scenarios. In our case we chose a low/medium/high set of scenarios, namely, SSP1-2.6, SSP2-4.5, and SSP5-8.5 (O'Neill et al. 2016). The SSP1-2.6 scenario approximately corresponds to the previous scenario generation Representative Concentration Pathway (RCP) 2.6, and was chosen as the low scenario for our study as it was designed to have a likely warming within the Paris Agreement target of below 2C warming level. SSP2-4.5, corresponds to RCP4.5, and was chosen as the medium scenario as it was designed as a middle-of-the-road scenario between the low and high ones. Regarding the high scenario, we had the choice of SSP3-7.0 vs SSP5-8.5, and we chose the latter because it corresponds to RCP8.5 that was used in V2, and is also likely to cover the upper end of the scenario uncertainty spectrum. Notably, as per the CORDEX experiment design for dynamical downscaling of CMIP6, SSP3-7.0 and SSP1-2.6 scenarios were chosen to be downscaled first, followed by additional downscaling using the SSP2-4.5 scenario and/or the SSP5-8.5 scenario based on the availability of computational resources.

A similar dynamical downscaling exercise is underway by the CORDEX-SEA community to produce high resolution climate change projections over SEA. There are several similarities and differences between the 2 efforts which make them highly complementary. Similarities include the choice of GCMs to be downscaled, large overlap in the downscaling domain and a common future scenario (SSP1-2.6). Differences include: (1) horizontal resolution (our downscaling is conducted at 8 km for SEA and 2km for WMC), whereas, most of the CORDEX-SEA downscaling will be carried out at 25 km horizontal resolution, (2) the N-S extent of our domains are very similar but our E-W extent is larger by around 20 degrees, (3) we use SSP5-8.5 as the high scenario, whereas CORDEX-SEA

uses SSP3-7.0, and (4) we use SINGV-RCM (Prasanna et al. 2023; submitted) and WRF (for a subset of the runs carried out using SINGV-RCM in order to assess downscaling uncertainty) as the downscaling model, whereas, CORDEX-SEA uses RegCM and WRF.

It is to be noted that while our intention was to sample as many family of models as feasible based on existing literature on model genealogy, we decided to have 2 models from one family (ACCESS-CM2 and UKESM1-0-LL) for 2 reasons: (1) the 2 models satisfied all our other criteria for model sub-selection, and (2) to analyse how similar or different can be the regional projections from 2 models of the same family, although they have different ocean models.

It is also to be noted that one of our final models that was used for downscaling (UKESM1-0-LL) has an ECS of 5.36oC which is beyond the very likely range of IPCC AR6 (2oC-5oC). Since we think it is important to span the range of ECS, provided the other sub-selection criteria are met, and the model being a credible GCM from the UKMO, we decided to go ahead with it.

In summary, we evaluated 49 CMIP6 GCMs for key climate variables and processes and using multiple dimensions of sub-selection we finally sub-selected 6 GCMs for dynamical downscaling over the 8 km SEA domain to produce the Third National Climate Change projections for Singapore.

References

Adler, R. F., G. J. Huffman, A. Chang, R. Ferraro, P. Xie, J. Janowiak, B. Rudolf, U. Schneider, S. Curtis, D. Bolvin, A. Gruber, J. Susskind, P. Arkin, and E. Nelkin, (2003) The version 2 Global Precipitation Climatology Project (GPCP) monthly precipitation analysis (1979-present). J. Hydrometeor, 4(6), 1147-1167.

Ashouri, H., Hsu, K.-L., Sorooshian, S., Braithwaite, D. K., Knapp, K. R., Cecil, L. D., et al. (2015). PERSIANN-CDR: Daily Precipitation Climate Data Record from Multisatellite Observations for Hydrological and Climate Studies. Bulletin of the American Meteorological Society, 96(1), 69–83. https://doi.org/10.1175/BAMS-D-13-00068.1

Bock, L., Lauer, A., Schlund, M., Barreiro, M., Bellouin, N., Jones, C., et al. (2020). Quantifying Progress Across Different CMIP Phases With the ESMValTool. Journal of Geophysical Research: Atmospheres, 125(21), e2019JD032321.

CORDEX (2021) (https://cordex.org/wp-content/uploads/2021/05/CORDEX-CMIP6_exp_ design _RCM.pdf; last accessed 09 Feb 2023)

Eyring, V., Bony, S., Meehl, G. A., Senior, C. A., Stevens, B., Stouffer, R. J., & Taylor, K. E. (2016). Overview of the Coupled Model Intercomparison Project Phase 6 (CMIP6) experimental design and organization. Geoscientific Model Development, 9(5), 1937–1958.

Fiedler, S., and Coauthors (2020) Simulated Tropical Precipitation Assessed across Three Major Phases of the Coupled Model Intercomparison Project (CMIP). Mon. Wea. Rev., 148, 3653–3680, https://doi.org/10.1175/MWR-D-19-0404.1.

Flynn, C. M., & Mauritsen, T. (2020). On the climate sensitivity and historical warming evolution in recent coupled model ensembles. Atmospheric Chemistry and Physics, 20(13), 7829–7842.

Gelaro, R., and Coauthors (2017) The Modern-Era Retrospective Analysis for Research and Applications, Version 2 (MERRA-2). J. Climate, 30, 5419–5454, https://doi.org/10.1175/JCLI-D-16-0758.1.

Hersbach, H, Bell, B, Berrisford, P, et al. (2020) The ERA5 global reanalysis. Q J R Meteorol Soc.; 146: 1999– 2049. https://doi.org/10.1002/qj.3803.

Hirahara, S., Ishii, M., and Y. Fukuda (2014) Centennial-scale sea surface temperature analysis and its uncertainty. J of Climate, 27, 57-75.

Huang, B., Peter W. Thorne, et. al. (2017) Extended Reconstructed Sea Surface Temperature version 5 (ERSSTv5), Upgrades, validations, and intercomparisons. J. Climate, doi: 10.1175/JCLI-D-16-0836.1

Huffman, G.J.; Bolvin, D.T.; Braithwaite, D.; Hsu, K.; Joyce, R.; Kidd, C.; Nelkin, E.J.; Sorooshian, S.; Tan, J.; Xie, P. (2019) NASA Global Precipitation Measurement (GPM) Integrated Multi-satellitE Retrievals for GPM (IMERG). In Algorithm Theoretical Basis Document (ATBD) Version 06; NASA/GSFC: Greenbelt, MD, USA.

Huffman, George J., Bolvin, David T., Nelkin, Eric J., Wolff, David B., Adler, Robert F., Gu, Guojun, Hong, Yang, Bowman, Kenneth P., Stocker, Erich F. (2007) The TRMM Multisatellite Precipitation Analysis (TMPA): Quasi-Global, Multiyear, Combined-Sensor Precipitation Estimates at Fine Scales. Journal of Hydrometeorology. Vol. 8, No. 1, pp. 38-55. DOI: 10.1175/JHM560.1 ISSN: 1525-755X, 1525-7541

Hurrell, J. W., J. J. Hack, D. Shea, J. M. Caron, and J. Rosinski (2008) A New Sea Surface Temperature and Sea Ice Boundary Dataset for the Community Atmosphere Model. Journal of Climate, 21, 5145–5153, https://doi.org/10.1175/2008jcli2292.1.

K. Okamoto, T. Iguchi, N. Takahashi, K. Iwanami and T. Ushio (2005) The global satellite mapping of precipitation (GSMaP) project, 25th IGARSS Proceedings, pp. 3414-3416.

Knutti, R., Masson, D., & Gettelman, A. (2013). Climate model genealogy: Generation CMIP5 and how we got there. Geophysical Research Letters, 40(6), 1194–1199. https://doi.org/10.1002/grl.50256

Kubota T et al. (2007) Global pecipitation map using satellite-borne microwave radiometers by the GSMaP project: production and validation IEEE Trans. Geosci. Remote 45 2259–75

Martin, G. M., Levine, R. C., Rodriguez, J. M., and Vellinga, M. (2021) Understanding the development of systematic errors in the Asian summer monsoon, Geosci. Model Dev., 14, 1007–1035, https://doi.org/10.5194/gmd-14-1007-2021.

McSweeney, C., Rahmat, R., Redmond, G., Marzin, C., Murphy, J., Jones, R., et al. (2015) Sub-selection of CMIP5 GCMs for downscaling over Singapore (Vol. 2).

Morice, C. P., J. J. Kennedy, N. A. Rayner, and P. D. Jones (2012) Quantifying uncertainties in global and regional temperature change using an ensemble of observational estimates: The HadCRUT4 dataset, J.

Geophys. Res., 117, D08101, doi:10.1029/2011JD017187.

Nguyen, P., E.J. Shearer, H. Tran, M. Ombadi, N. Hayatbini, T. Palacios, P. Huynh, G. Updegraff, K. Hsu, B. Kuligowski, W.S. Logan, and S. Sorooshian (2019) The CHRS Data Portal, an easily accessible public repository for PERSIANN global satellite precipitation data, Nature Scientific Data, Vol. 6, Article 180296. doi: https://doi.org/10.1038/sdata.2018.296

Power, S., F. Delage, C. Chung, G. Kociuba, and K. Keay (2013) Robust twenty-first-century projections of El Niño and related precipitation variability. Nature, 502, 541–545, https://doi.org/10.1038/nature12580.

Rayner, N. A., Parker, D. E., Horton, E. B., Folland, C. K., Alexander, L. V., Rowell, D. P., Kent, E. C., and Kaplan, A. (2003) Global analyses of sea surface temperature, sea ice, and night marine air temperature since the late nineteenth century, J. Geophys. Res., 108, 4407, doi:10.1029/2002JD002670, D14.

Reynolds, Richard W., Thomas M. Smith, Chunying Liu, Dudley B. Chelton, Kenneth S. Casey, Michael G. Schlax (2007) Daily High-Resolution-Blended Analyses for Sea Surface Temperature. J. Climate, 20, 5473-5496.

Roca, R., Alexander, L. V., Potter, G., Bador, M., Jucá, R., Contractor, S., et al. (2019) FROGS: a daily 1° × 1° gridded precipitation database of rain gauge, satellite and reanalysis products. Earth System Science Data, 11(3), 1017–1035. https://doi.org/10.5194/essd-11-1017-2019.

Rohde, R. A. and Hausfather, Z.: (2020) The Berkeley Earth Land/Ocean Temperature Record, Earth Syst. Sci. Data, 12, 3469–3479, https://doi.org/10.5194/essd-12-3469-2020.

Sadeghi, M., Nguyen, P., Naeini, M. R., Hsu, K., Braithwaite, D., & Sorooshian, S. (2021) PERSIANN-CCS-CDR, a 3-hourly 0.04° global precipitation climate data record for heavy precipitation studies. Scientific Data, 8(1), 157. https://doi.org/10.1038/s41597-021-00940-9.

Shinya KOBAYASHI, Yukinari OTA, Yayoi HARADA, Ayataka EBITA, Masami MORIYA, Hirokatsu ONODA, Kazutoshi ONOGI, Hirotaka KAMAHORI, Chiaki KOBAYASHI, Hirokazu ENDO, Kengo MIYAOKA, Kiyotoshi TAKAHASHI (2015) The JRA-55 Reanalysis: General Specifications and Basic Characteristics, Journal of the Meteorological Society of Japan. Ser. II, Volume 93, Issue 1, Pages 5-48, Released on J-STAGE March 18, 2015, Online ISSN 2186-9057, Print ISSN 0026-1165, https://doi.org/10.2151/jmsj.2015-001

Xie P., Joyce R., Wu S., Yoo S.-H., Yarosh Y., Sun F. and Lin R. (2017) Reprocessed, bias-corrected CMORPH global high-resolution precipitation estimates from 1998 J. Hydrometeorol. 18 1617–41.

Appendix

A5.1 Evaluations for seasonal rainfall

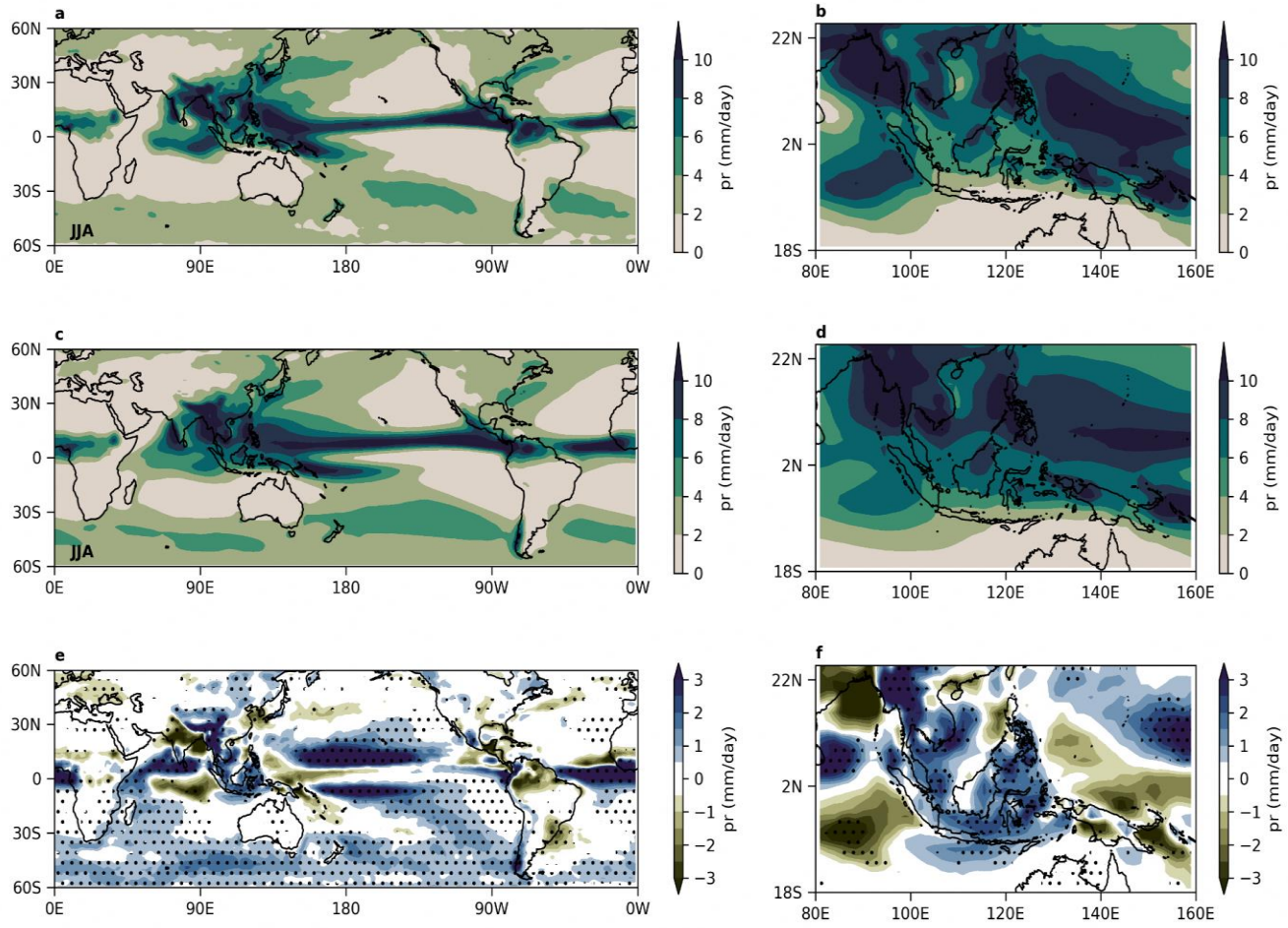

Figure A5.1: 1995-2014 JJA season mean precipitation (pr) in observation (a,b) and models (c,d). a. FROGS datasets for the 60N-60S domain. b. similar to a, but for the SEA domain. c. multi-model mean of pr from 48 CMIP6 models for the 60N-60S domain. d. similar to c, but for the SEA domain. e. model bias (e.g., multi-model mean from 48 models minus the observational mean). Stippled areas indicate the agreement by 70% of models. f. similar to e, but for the SEA domain.

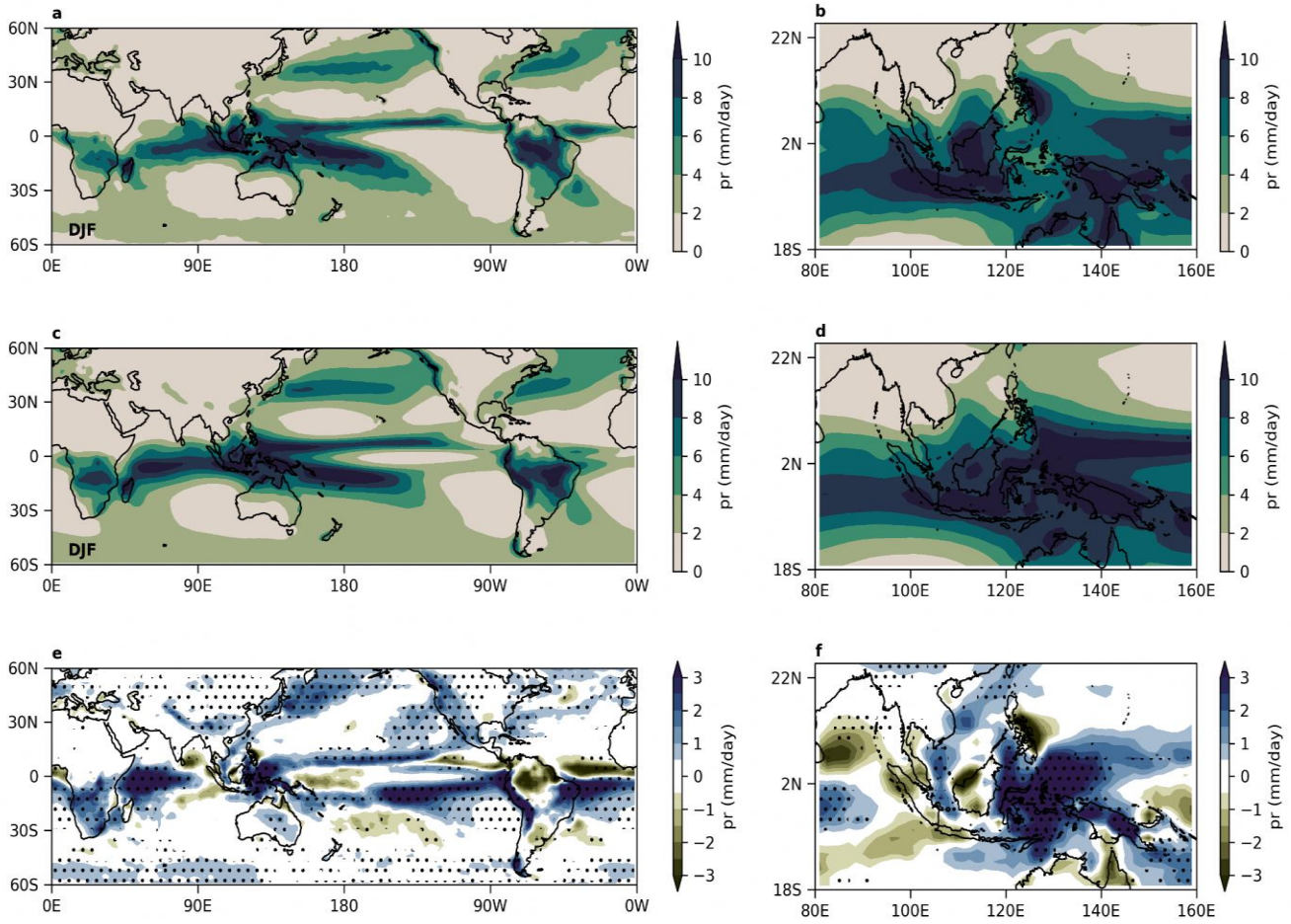

Figure A5.2: 1995-2014 DJF season mean precipitation (pr) in observation (a,b) and models (c,d). a. FROGS datasets for the 60N-60S domain. b. similar to a, but for the SEA domain. c. multi-model mean of pr from 48 CMIP6 models for the 60N-60S domain. d. similar to c, but for the SEA domain. e. model bias (e.g., multi-model mean from 48 models minus the observational mean). Stippled areas indicate the agreement by 70% of models. f. similar to e, but for the SEA domain.